Gnamma Pit Growth and Paleowind Intensity in the Sonoran Desert:

Insights from Wind Tunnel Experiments and Numerical Modeling

by

Yinlue Wang

A Thesis Presented in Partial Fulfillment
of the Requirements for the Degree
Master of Arts

Approved April 2015 by the
Graduate Supervisory Committee:

Mark Schmeeckle, Chair
Ronald Dorn
Robert Balling

ARIZONA STATE UNIVERSITY

May 2015

ABSTRACT

Gnamma pit is an Australian aboriginal term for weathering pit. A mix of weathering and aeolian processes controls the formation of gnamma pits. There is a potential to utilize gnamma as an indicator of paleowind intensity because gnamma growth is promoted by the removal of particles from gnamma pits by wind, a process referred to as deflation. Wind tunnel tests determining the wind velocity threshold of deflation over a range of pit dimensions and particles sizes are conducted. Computational fluid dynamics (CFD) modeling utilizing the Re-Normalisation Group (RNG) K-Epsilon turbulence closure is used to investigate the distribution of wall shear stress and turbulent kinetic energy. An empirical equation is proposed to estimate shear stress as a function of the wind velocity and pit depth dimensions. With this equation and Shields Diagram, the wind velocity threshold for evacuating particles in the pit can be estimated by measuring the pit depth ratio and particle size. It is expected that the pit would continue to grow until this threshold is reached. The wind speed deflation threshold is smaller in the wind tunnel than predicted by the CFD and Shields diagram model. This discrepancy may be explained by the large turbulent kinetic energy in the gnamma pit as predicted by the CFD model as compared to the flat bed experiments used to define the Shields diagram. An empirical regression equation of the wind tunnel data is developed to estimate paleowind maximums.

TABLE OF CONTENTS

LIST OF TABLES

LIST OF FIGURES

Figure Page

Chapter 1

INTRODUCTION

Gnamma pit is an Australian aboriginal term for weathering pit. Weathering pits are widely reported in low temperature environments (Fahey 1986) and arid surroundings (Laity 2009), Weathering pits develop on a whole range of rocks, however, they are especially profuse on granite substrates (Twidale 1965).

As is the case for some other geomorphologic landscapes caused by erosion, gnamma formation is driven by a positive feedback. First, water collects in a small depression when precipitation happens. Second, weathering processes decay the grain contacts to the point where granular disintegration occurs. Third, wind blows the grains out of the pit, enlarging the pit and allowing it to collect more water (Twidale 1965; Hall and Phillips 2006; Domínguez-Villar et al. 2008). While the depth of gnammas would not increase indefinitely, a spillway would develop and finally breach the whole pit, or sediments can be deposited on the pit when erosion is not as strong as before. Many researchers have focused on weathering processes, especially chemical weathering. However, there is a lack of study of the aeolian component of gnamma formation. I seek the relationship between wind intensity and gnamma morphology and consider gnammas as landscapes formed by aeolian transportation and weathering processes.

Weathering pits are complicated in form, and geomorphologists have tried to find a better way to measure and define the shape of gnammas. Twidale (1965) discussed the 3 distinct forms of gnammas in different settings: pans, pits, and armchair-shaped hollows, by recognizing different cross-section profiles. Domínguez-Villar (2006) developed a quantitative measurement for gnammas and defined more types of gnammas by appearance. In his research, Domínguez-Villar (2006) measured

depression depth, the minimum height or spillway height, length, width, area, volume, and depth ratio (minimum depth/maximum depth).

A trend from qualitative observation to quantitative measurement can be found in the progress of weathering pit research. A particularly important approach is Gnamma Morphometric Analysis (GMA), that divides the gnamma population of a research site into smaller groups according to different depth ratio values (Domínguez-Villar 2006) . Some later studies (Domínguez-Villar and Jennings 2008; Tian et al. 2013) utilized GMA in their morphometric analyses.

Weathering geomorphology plays a critical role in weakening bedrock to allow gnamma genesis and development. Weathering geomorphology studies weathering process in landscapes. Rocks and minerals break down through contact with the atmosphere and water as well as by bioturbation. In general, weathering reactions are controlled by temperature (thermal stress), moisture (direct precipitation, salt weathering), and biological activities (Smith 2009). If a weathering pit is active, and is not covered with thick soils, the rock surface would be exposed to the atmosphere and water, which results in a continuous cycle of exposure to water and then exposure to air upon the evaporation of water.

Generally, bioturbation is not as significant as other weathering factors in gnamma weathering, because these pits appear on vegetation-free rocks, and because there is not much interaction between rock surfaces and animals in arid or cold areas. Physical weathering is caused by a change of physical condition, and it includes direct contact (e.g., rain drops) and indirect factors (e.g., thermal stress). The freeze-thaw or heat-cool cycle would ultimately destroy the rock structure and break the rock surface into small particles (Fahey 1986). As Smith (2009) pointed out, some salt weathering processes also belong to physical weathering, because salt crystals formed in preexisting cracks by can expand when exposed to higher humidity, thus causing the cracks to grow.

Using digital processing of back-scatter electron (BSE) images, Dorn (1995) studied the fine details of how gnamma pit grains decay in Hawaii. He suggested that gnamma formation of weathering is a positive feedback. First, a glaze covers the surface, but physical weathering occurs in the subsurface that is under the glaze. Weathering processes decay the grain underneath the glaze and enlarge the porosity. When the porosity is large enough, the surface breaks into particles and particles spall off. A new glaze forms in the "fresh surface," that continues the cycle. This process is more efficient than direct weathering processes, and it is similar with Twidale's (1965) hypothesis.

Dissolution is the most well-known process in chemical weathering. Working in higher elevations, Fahey (1986) thought that chemical weathering plays a very little role in pit formation. He used field observation and chemical analysis to show that there was not a significant change in ions. Therefore, he suggested that chemical weathering is not important in high altitudes. Still, there are also studies with detailed observations and experiments supporting the importance of chemical weathering in the formation of gnammas. Domínguez-Villar et al. (2008) used quantitative experiments to derive diurnal and seasonal changes of chemical characteristics in the water collected by gnammas. A clear change of concentration of oxygen, carbon dioxide, and pH can be seen in their experimental results. Also, field observations show a seasonal change of conductivity, ORP (redox potential). Finally, Domínguez-Villar (2008) thought that weathering processes are even noticeable during the winter, when water overflow can chemically enrich solutions trapped in the depressions. Tian et al. (2013) applied the same method in northern China. They also found that chemical processes help weaken grains and promote gnamma genesis, especially salt weathering. Thus, the relative importance of physical versus chemical processes appears to vary geographically with alpine gnamma growth supported by physical weathering and desert growth supported by chemical decay of the host rock.

Characteristics of weathering processes in warm deserts include: (1) weathering processes are likely to be distinctive because of distinctive fluctuation of diurnal and seasonal temperature and relative humidity; (2) moisture for weathering is widely available, from rainfall, dew, and fog, which is contrary to popular belief; and (3) physical processes are probably significantly more important than elsewhere, but the role of chemical processes should not be ignored (Cooke et al. 1993).

Although gnamma pits are generally considered weathering landforms, the most important role of weathering in weathering pit formation is to turn bedrock into debris that is then transported by wind. Aeolian erosion refers the erosion caused by wind, and it is significant in vegetation-free areas. Therefore, aeolian processes are important in desert geomorphology, coastal geomorphology, and planetary geomorphology. Laity (2009) made a summary of aeolian erosion in deserts. Aeolian erosion processes receive less attention from geomorphologists than aeolian deposition landscapes, such as sand dunes. Aeolian erosion surfaces contain abrasions and deflations, and the rocks eroded by winds are called ventifacts. Because they are made from different rock types, ventifacts have different forms: facets, pits, flutes, scallops, grooves, etc.

No prior literature review focused on the role of wind in gnamma pit growth. Netoff and Chan (2009) studied a sandstone weathering pit that was meters deep in Utah and described evidence for the role of aeolian activity in the huge pit, but there was no theory development from their research.

Because of the lack of direct study of wind systems interacting with small depressions, I turn to the broader literature where aeolian geomorphologists constructed models and hypotheses with the field data or experiments. Walker and Nickling (2002) generated the basic theory of flow over the lip of a depression. Holcombe et al. (1997) used a time series analysis of the wind intensity from 1948 to 1978 and the response of dust to wind. The research showed that the threshold mean hourly wind speeds (MHWSs)

would be increased after prior precipitation because of impacts to canopy and source area. Fluid dynamic modeling is an efficient way to consider the aeolian processes for this erosion is driven by airflow. Hesp and Hyde (1996) applied dynamic methods to study the aeolian formation of blowouts — sandy depressions in a sand dune. This research tested data simulated by dynamic simulation with field observation and presented different formation processes of blowouts with different morphology. These blowouts are analogous to gnamma pits, because the nature of wind flow over blowout depressions can provide useful models for analyzing weathering pits.

Wind tunnels provide an opportunity to simulate the influence of wind on landforms. Greeley et al. (1974), for example, used wind tunnel experiments to test the hypothesis of aeolian processes on Mars. They simulated Martian conditions in a wind tunnel, conducted experiments about aeolian sediment transportation, compared the experimental results with image of landscape on Martial surface, and finally found the threshold for grain movement on Mars. Ward and Greeley (1984) studied the development of yardangs (elongate wind-eroded ridges that develop at various scales) with wind tunnels, and they discussed distribution of pressure and wind velocity in the surface of yardangs. Wind tunnels can also provided an improved understanding of aeolian thresholds (Stout, 1998). Stout (1998) utilized a wind tunnel experiment and found that the threshold of the wind speed for sediment saltation decreased with increasing of proceeding time.

Numerical simulation methods are involved in contemporary studies. Computational fluid dynamics (CFD) models simulate aeolian processes according to equations describing the continuity of mass, momentum, and energy. Parsons et al. (2004) came up with a CFD model for the formation and alteration of transverse dunes. The authors also used wind tunnel experiments to validate the model; wind tunnel experiments cannot provide detailed information of turbulence and flow reversal due to

technical deficiencies, however, it is a good way to test the validity of models. Jackson et al. (2011) built a 3-D CFD model for sand dune in coastal area with the parameters obtained by ultrasonic anemometry. Their model provided new insight into offshore sand dune formation.

Ventifacts are formed by aeolian erosion. As such, the study of aeolian landscapes can produce a better understanding of paleowind profiles. Paleowind direction can be determined from the orientation of facets (Laity 1987). Rock varnish on ventifacts can also provide an aeolian record with a reliable dating result (Dorn 1986). Many researchers chose yardangs to extract a wind profile (Ward and Greeley 1984; Gutiérrez-Elorza 2002; Goudie 2007; Sebe 2011). A gnamma is formed by aeolian erosion, that shows a potential for extracting paleowind history with a relative age (Hall and Phillips 2006).

Chapter 2

METHODS

This research on gnamma pits and paleowind determination includes laboratory experiments, numerical computations, and field measurements. Laboratory experiments were conducted to determine the wind intensities needed to deflate grains from an idealized shallow-bowl-shaped gnamma pits. These full-scale experiments were used to link with fluid dynamic models of how wind flows across these shapes. The output of the wind tunnel experiment and numerical modeling produced a relationship between wind speed and particle deflation for different grain sizes — all with this idealized shape of a shallow bowl. The last part of the work then took this output into the field; using only natural gnamma pits with this shape, I estimated wind thresholds needed to enlarge these pits.

Wind Tunnel Experiments

Full-scale simulation experiments were run in the wind tunnel of the Ronald Greeley Center for Planetary Studies, Arizona State University. Three idealized shapes (e.g., shallow bowls) flush with the surface of the wind tunnel were placed, which created the opportunity to collect the wind intensity (threshold) needed to deflate different sized particles from these idealized shapes. Grus sands from the Sonoran Desert were used in experiments, and they were sieved into five ranges of grain size (4mm, 2mm, 0.5mm, 0.25mm, 0.125mm). The sieving process and different molds constructed a matrix made up of three shape parameters and five particle sizes, by putting a single-grain layer of grus on the bottom of the plates. Then, different combinations of molds with different depths and sediments in the wind tunnel were tested. The threshold of sediment motion under unidirectional currents is somewhat arbitrary and difficult to determine (Miller et al. 1977). Here the threshold of each set was decided by observing whether there is

obvious particle movement at the bottom of the molds. I therefore measured the threshold needed to transport the particles from these molds as wind intensity was slowly increased in the wind tunnel and motion of bottom sediment was observed.

Computational Fluid Dynamics Modeling

OpenFOAM (Open Source Field Operation and Manipulation) was used to simulate the incompressible turbulent flow in the wind tunnel. A two-dimensional model of the wind flow along a vertical and downwind plane through the center of a pit was conducted by solving the Reynolds-averged Navier Stokes (RANS) equations. The Reynolds stresses were modeled by the re-normalisation group (RNG) k-epsilon model, developed by Yakhot et al. (1992). A steady state solver called SimpleFoam was utilized to simulate the steady state of incompressible flows. Meshes for the CFD simulations were set with the equivalent shape of the three molds of the wind tunnel in experiments. The kinematic viscosity was set to $1.5\times10^{-5}\ m^2/s^2$ (the value under the temperature around 300K). Graphs of the distribution of velocity, wall shear stress, and turbulent kinetic energy were displayed via OpenFOAM. Values can also be extracted by "sample utility" provided by OpenFOAM, which gathered data for further comparison and analysis.

Fieldwork and Study Site Context

Although aeolian features like sand dunes occur in isolation, gnamma pits are ubiquitous features and an understanding of wind flow could allow mapping of paleowind intensities over a large area. The Phoenix metropolitan area was selected for the investigation into the winds needed to enlarge gnamma pits for the reason that granitic bedrock with gnamma pits exists in abundance there and it is possible to find granitic outcrops that are above the surrounding vegetation and that would just encounter winds without increased roughness effects imposed by plants. Also, aeolian

process plays an important role in arid environments as mentioned. The survey was conducted in the McDowell Mountains and South Mountains.

The ultimate goal of this research is to better understand ancient winds, providing a new view of climate change dynamics. Fieldwork linked theoretical modeling work and wind tunnel experiments to paleoclimatology. I made measurement for four weathering pits in McDowell Mountain and eleven pits in South Mountains. Complex and irregular gnammas were considered as simplified oval shapes in measuring morphologic parameters. I measured the depth (h), length of upper major axis (w1), length of bottom major axis (w2), direction of major axis, length of upper minor axis, length of bottom minor axis, direction of minor axis, longitude, and latitude of all the samples. The depth-to-width ratio was calculated as $\delta = 2h/(w1 + w2)$, (i.e., depth over the mean length of the major axes).

The fieldwork focused on pits that have stopped deflating, and those pits whose grain sizes are too big to deflate were calculated according to the simulation results. Sediment in the pits was collected. Particles larger than 0.5mm were used for grain size statistics. Three sieves (4mm, 2mm, 0.5mm) were utilized to separate the grains from each pit. Percentages of different grains (D15, D50, D85) were thus estimated for each pit. After morphological and granular parameters were obtained, I extracted the paleowind threshold with the aid of the relationship between gnamma parameters and wind speed extracted by the experiments and numerical modeling.

Chapter 3

RESULTS

Laboratory

Corresponding wind speed intensities necessary for blowing particles out of pits were obtained by the wind tunnel experiments. For 45 mm deep mold, the largest particles (4mm) were stable when wind velocity rose from 0 to 20 meters per second. When 2mm grains were placed in the mold, an obvious shifting process can be noted in the wind speed of 16.1 meters per second. However, no particles were blown out of the pit. There was also a noticeable movement of 0.5mm particles, and first motion out from the mold can be found when the wind speed was equal to 18.8 meters per second. 0.25mm particles began to creep at the wind velocity of 6.8 meters per second, and be blown out at the speed of 15 meters per second. 0.125mm grus crept downwind at the speed of 12 meters per second, and grus would be blown out when the velocity was above 13 meters per second. Particles placed in the mold of median depth moved in relatively lower wind speed. Particles of 4mm and 2mm could not be blown out if wind speed was less than than 20 meters per second, but a motion of 4mm particles could be seen when wind speed reached 17 meters per second. 0.5mm particles moved with a 12 meters per second wind, and were evacuated under 15.3 meters per second airflow. Before being blown out when velocity was 10.7 meters per second, 0.25mm grus would creep at the speed of 6.7 meters per second. For 0.125mm particles, they moved out of the molds when wind speed was 10 meters per second. 12mm plate is the shallowest mold in experiments. 4mm particles in situ would shift at the velocity of 14.9 meters per second while they were still in the mold when speed is below 20 meters per second. 2mm grus shifted under 9.5 meters per second wind, and was removed under 15.1 meters per second. Shifting speed of 0.5mm particles was 6.2 meters per second, and the wind

intensity required to blow out that particle was 9.9 meters per second. 0.25mm particles crept when wind velocity reached 8 meters per second and were blown out under 8.3 meters per second. 0.125mm particles' wind threshold was 8 meters per second.

Depending on the phenomena, wind thresholds needed to evacuate particles were summarized (Table 1). Particles are most stable at speed of 20 m/s when there is a combination of a deep mold and large particles. Deeper pits require a more intense wind to remove a particle of a given size. In shallow (12mm) molds particles can only reach the stable status in 20 meters per second later when there are the largest biggest (4mm) in the pit. For median (21mm) and deep (45mm) molds, particles are stable when their grain size is 2mm. In addition, it is possible to compare the threshold needed to deflate same sized particles in different molds. The gathered data reveals that grain size is a significant factor influencing the wind speed needed to deflate particles from a gnamma pit. A substantial difference exists between thresholds of 4mm particles and 0.125 particles. For largest grains, wind speed cannot be measured, while for 0.125mm sediments they are less than 13 meters per second.

Table 1. Measured wind threshold (m/s) from wind tunnel experiments

Pit depth (mm) / Grain size (mm)	12	21	45
4	>20	>20	>20
2	15.1	>20	>20
0.5	9.9	15.3	18.8
0.25	8.3	10.7	15
0.125	8	10	13

Note: 20m/s is the maximum speed in this condition, which means the actual wind threshold of some sets is higher than 20m/s.

Numerical Simulation

Twenty-four model simulations were performed. They were utilized to obtain the distribution of shear stress, turbulent kinetic energy and velocity of the pits used in the wind tunnel experiments. Steady-state solutions for incompressible, turbulent airflow in varying wind speed over different gnammas were calculated. Similar flow structures were found in all of the different conditions. The flow field is divided into different parts, and a boundary layer is formed above the floor of the wind tunnel. Re-distribution of wind velocity is also apparent in the tunnel due to airflow separation. Flow separation occurs at the leading edge of the pit, giving rise to flow recirculation in the pit.

Wall shear stress of each boundary cell was calculated. Figure 1 shows that the shear stress on the floor increases from inlet to outlet, and then decreases. The maximum shear stress is located closer to inlet end of the pit, rather than outlet. A relationship between wind velocity (u) and shear velocity (u*) was derived from the CFD simulations of maximum shear stress at the floor of the pit. Three linear regressions were made for three corresponding shapes (Figure 2) based on the assumption that shear stress can only be zero when there is no wind. According to R-squareds (0.9993 for 12mm mold, 0.9991 for 21mm mold, and 0.9964 for 45mm mold), linear regression is adequate here.

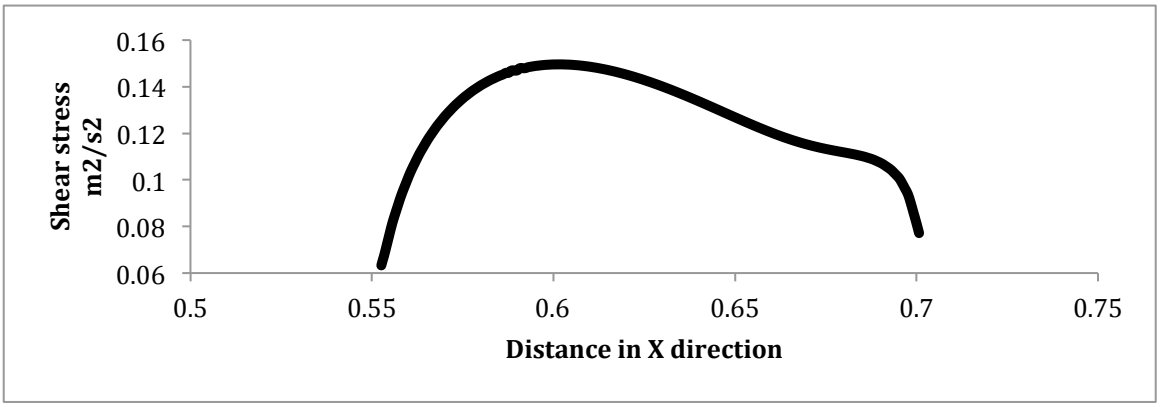

Figure 1. Wall shear stress of the bottom of 20m/s wind flow over 45mm pit

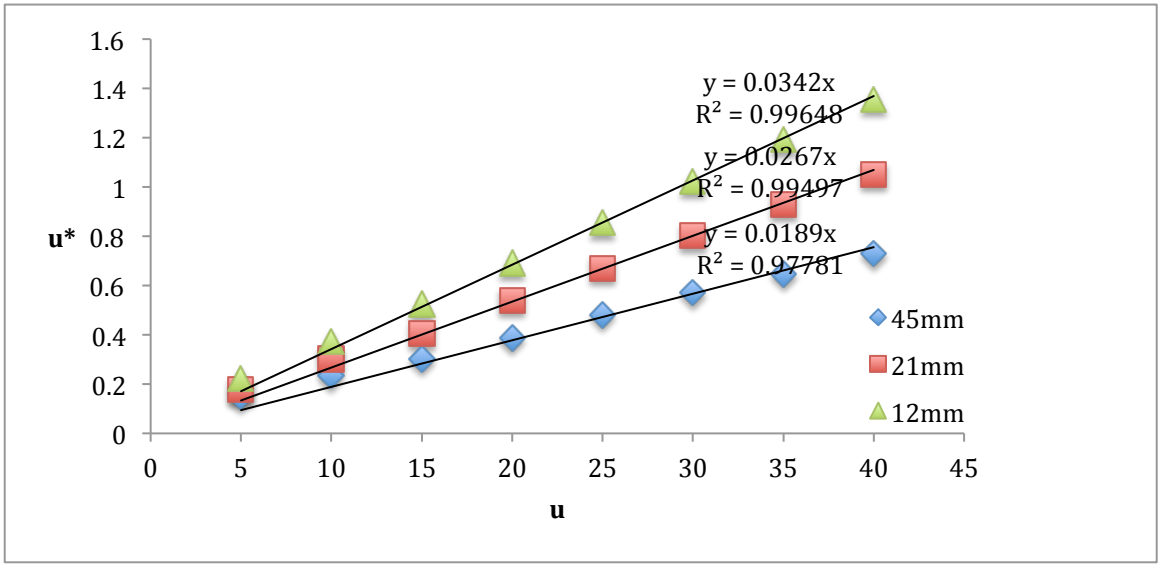

Figure 2. Relationship between wind velocity (u) and maximum shear velocity (u*) derived from CFD model of maximum shear stress at the floor of the pit

In order to couple linear regression equations from each mold, a multiple factors regression was made and depth-to-width ratio was used. The depth-to-width ratio, calculated as

$\delta = 2h/(w1 + w2)$, offered a better regression fit than multi-factor regression between wind speed and mold depth. The multi-factor regression result is

$$\frac{u*}{u} = \frac{1}{90.83\delta^{0.4189}} \quad (1)$$

with an R-squared of 0.7847 and p-value lower than 0.01. Based on this equation, the shear velocity to wind velocity ratio can be estimated by the depth-to-width ratio of gnammas.

The turbulent kinetic energy (k) was also obtained from RNG k-epsilon models. Profiles are shown in Appendix A.

Fieldwork

Four samples were selected from McDowell Mountain, Scottsdale. Pit depth ranged from 2.1cm to 10.2cm, with a mean value of 4.9cm and a median value of 3.65cm. Eleven pits were sampled from South Mountains, Phoenix. Pit depth ranged from 1.3cm to 8.7cm, with a mean value of 2.61cm and a median value of 2.2cm. Morphologic profiles were shown as Table 2. Grain size information was also collected, and grain size percentiles were calculated (Table 3). All the D15 values are 0.5mm. But, pits in McDowell Mountain contain larger particles, considering both the D50 and D85 values.

Threshold Estimation Using Shields Diagram

The regression (Equation 1) and field data were used to estimate u/u* was for each sample pit. Combined with the Shields diagram (Shields 1936), wind speed for sediment incipient motion can be estimate. According to Cao et al. (2006):

$$\tau_{*c} = 0.045 \; when \; D_* \geq 282.84$$

$$\tau_{*c} = \frac{(1+(0.0223D_*)^{2.8358})^{0.3542}}{3.0946D_*^{0.6769}} \; when \; 6.61 < D_* < 282.84 \qquad (2)$$

$$\tau_{*c} = 0.1414D_*^{-0.2306} \; when \; D_* \leq 6.61$$

where

$$D_* \equiv \frac{\sqrt{\left(\frac{\rho_s}{\rho} - 1\right) g D^3}}{\nu}$$

The critical shear velocity for incipient motions of given particles, u*c, would be estimated from Equation 2 using $\tau_{*c}(\rho_s - \rho)gD = \rho u_{*c}^2$. The corresponding wind velocity threshold can be found in Table 4 and Table 5.

Table 2. Location and morphology of gnamma samples

Pit number	Longitude	Latitude	Major axis			Minor axis			Depth (cm)	Depth-to-width ratio
			Direction	Upper length (cm)	Bottom length (cm)	Direction	Upper length (cm)	Bottom length (cm)		
M01	111°48.419'	33°40.749'	175° - 355°	61	37	55° - 235°	50	34	4.1	0.084
M02	111°48.625'	33°40.831'	150° - 330°	60	40.5	43° - 223°	57	26.4	10.2	0.203
M03	111°48.371'	33°40.798'	123° - 303°	23.1	18.5	34° - 214°	12.6	7.4	2.1	0.101
M04	111°48.369'	33°40.801'	25° - 205°	51.2	37.4	116° - 296°	29.5	18.2	3.2	0.072
S01	112°01.899'	33°21.949'	34° - 214°	29.4	12	135° - 315°	17	9.2	1.4	0.068
S02	112°01.865'	33°21.892'	98° - 278°	36.8	20	175° - 355°	17.4	10.8	1.4	0.049
S03	112°01.858'	33°21.871'	100° - 280°	16	8.8	6° - 186°	9	3.2	1.3	0.105
S04	112°01.837'	33°21.869'	125° - 305°	50.8	18	35° - 215°	21.8	12.4	8.7	0.253
S05	112°01.759'	33°21.810'	120° - 300°	16.8	12	20° - 200°	9	3.8	2.6	0.181
S06	112°01.759'	33°21.810'	80° - 260°	13.4	9.6	160° - 340°	6.6	3	1.9	0.165
S07	112°01.754'	33°21.792'	60° - 240°	7.8	3	3° - 183°	7	2	2.6	0.481
S08	112°01.727'	33°21.818'	0° - 180°	18	14	103° - 283°	17	13.2	2.3	0.144
S09	112°01.710'	33°21.804'	72° - 252°	31	15	160° - 340°	19.6	12	2.2	0.096
S10	112°01.710'	33°21.804'	60° - 240°	41	24.4	160° - 340°	14.4	10.8	2.6	0.08
S11	112°01.693'	33°21.803'	30° - 210°	44	25	125° - 305°	33	24	1.7	0.049

Note: M01-M04 refer to 4 pits in McDowell Mountain, and S01-S11 refer to 11 pits in South Mountain.

Table 3. Particles distribution of samples

Pit number	Particle distribution			Grain size percentiles (mm)		
	0.5	2	4	D15	D50	D85
M1	33.96%	41.51%	24.53%	0.5	2	4
M2	21.74%	40.58%	37.68%	0.5	2	4
M3	23.76%	53.47%	22.77%	0.5	2	4
M4	24.66%	57.53%	17.81%	0.5	2	4
S1	87.36%	12.64%	0.00%	0.5	0.5	0.5
S2	61.04%	27.61%	11.35%	0.5	0.5	2
S4	86.28%	8.86%	4.86%	0.5	0.5	0.5
S5	37.04%	44.44%	18.52%	0.5	2	4
S6	23.08%	55.38%	21.54%	0.5	2	4
S7	21.31%	32.79%	45.90%	0.5	2	4
S8	80.18%	14.77%	5.04%	0.5	0.5	2
S10	31.08%	27.03%	41.89%	0.5	2	4

Table 4. Required shear velocity for given particles according to Cao et al. (2006)

D (mm)	D*	τ*c	u* (m/s)
0.5	110.67	0.034	0.61
2	885.44	0.045	1.41
4	2504.39	0.045	1.99

Table 5. Required wind velocity and shear velocity of each pit

Pit number	δ	u*/u	D15's u*	D15's u	D50's u*	D50's u	D85's u*	D85's u
M01	0.084	0.031	0.61	19.63	1.41	45.34	1.99	64.04
M02	0.203	0.021	0.61	28.41	1.41	65.62	1.99	92.68
M03	0.101	0.029	0.61	21.21	1.41	48.98	1.99	69.18
M04	0.072	0.033	0.61	18.40	1.41	42.50	1.99	60.04
S01	0.068	0.034	0.61	17.97	0.61	17.97	0.61	17.97
S02	0.049	0.039	0.61	15.66	0.61	15.66	1.41	36.18
S04	0.253	0.020	0.61	31.15	0.61	31.15	0.61	31.15
S05	0.181	0.023	0.61	27.08	1.41	62.54	1.99	88.33
S06	0.165	0.023	0.61	26.05	1.41	60.16	1.99	84.97
S07	0.481	0.015	0.61	40.78	1.41	94.18	1.99	133.02
S08	0.144	0.025	0.61	24.60	0.61	24.60	1.41	56.83
S10	0.080	0.032	0.61	19.23	1.41	44.42	1.99	62.75

Chapter 4

DISCUSSION

Gnamma-Wind-Sediment Interaction

All of the data, graphs, and empirical equations show a positive relationship between wind speed threshold to deflate particles and particle size and pit depth. Gnamma pit geometry produces flow separation and recirculation in the pit. The flow pattern is similar to flow patterns in the leeward portion of transverse sand dunes (Walker and Nickling, 2002). Numerical results show that gnamma pits with a higher depth-to-width ratio have increased turbulent kinetic energies in the gnamma pits, which reduces the shear stress necessary to move particles. Particle size is another important factor of aeolian sediment transport processes. Larger grain size contributes to greater particle Reynolds numbers and requires corresponding larger shear stress when critical shear stress remains same value.

Grus inside gnammas in desert area is under the condition called “Transport limited” by Kirby (1971), which suggests that sediment transport rate is equal to sediment transport capacity. As mentioned, weathering processes are severe in arid environment due to a wide diurnal cycle of temperature. Depressions in rock surfaces have reduced boundary shear stresses, because of flow separation and recirculation; therefore particles are difficult to be entrained. This also explains why there is usually a thin layer of grus on the bottom of gnammas.

Influence of Turbulent Kinetic Energy and Calibration

Experimental values of transport threshold using CFD model estimates of shear stress are compared to Shields' curve. All available ten points have critical stresses less than the Shields curve as approximated by the equations of Cao et al. (2006). This

suggests that wall shear stress that removed particles is less than critical shear stress required of the Shields curve (Figure 3). The modeled turbulent kinetic energy (k) profile above the pit floor for three relative pit depth conditions (45mm/0.005mm, 21mm/0.005mm, 12mm/0.005mm) were selected. These three cases had similar Reynolds numbers and critical shear stress. Compared with Grass (1971), normalized turbulent kinetic energy ($\frac{\sqrt{k}}{u*}$) in a pit is higher than that on a flat bed, especially not far away from the bottom (Figure 4). Therefore, higher k value at the bottom might be a reason why particles in gnammas are removed more easily than data derived from flat flume experiments.

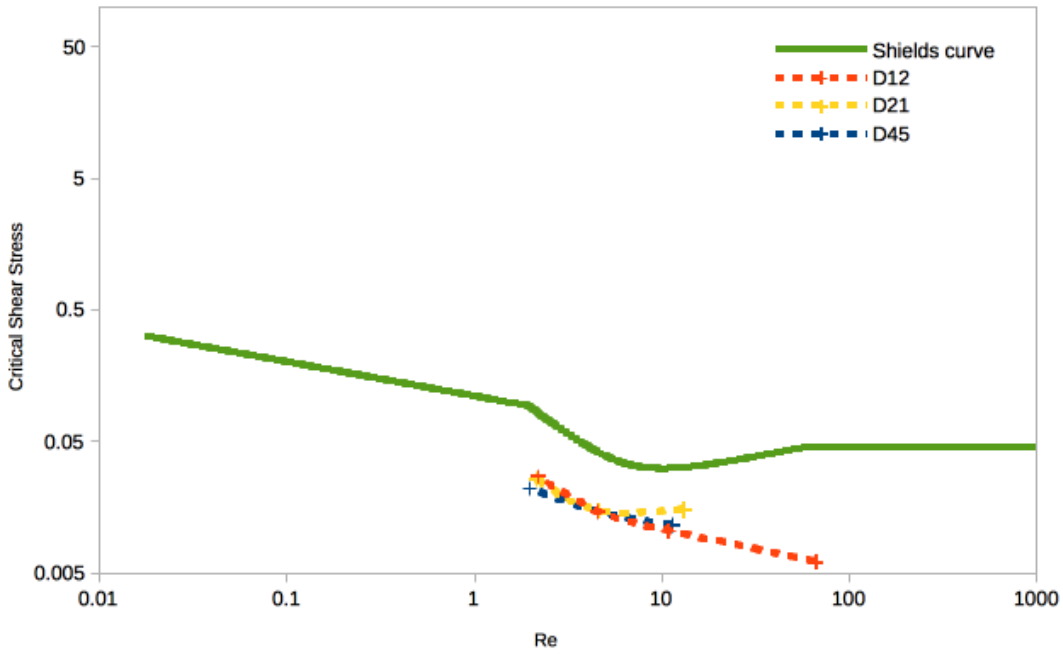

Figure 3. Experimental values of transport threshold using CFD model estimate of shear stress. Results are compared to Shields' curve.

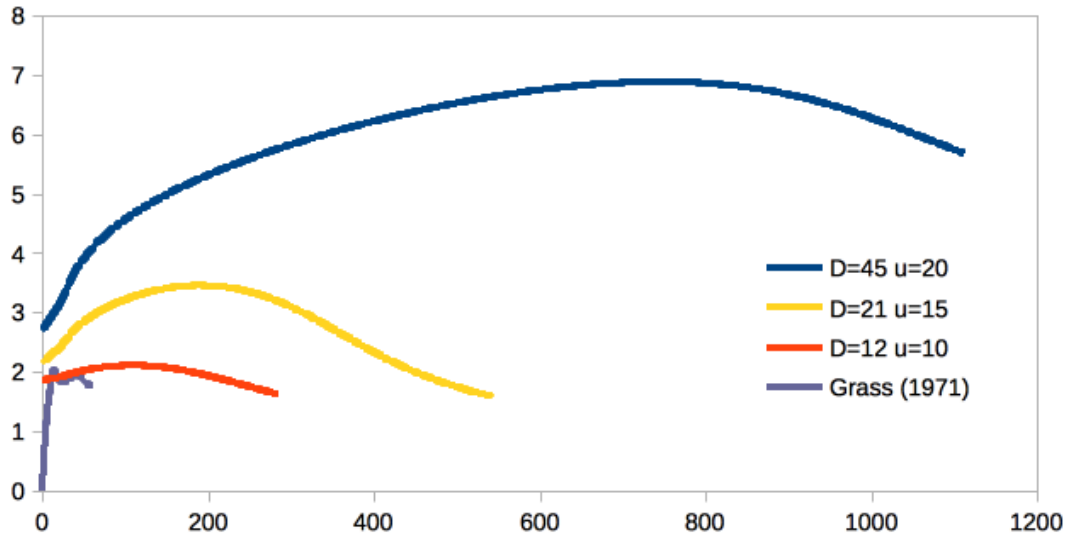

Figure 4. Modeled turbulent kinetic energy (k) profile above the pit floor for three relative pit depth conditions. These three cases had similar Re numbers and critical shear stress. Results are compared to Grass (1971).

Table 6 shows the ratio ($\tau c^{*'}/ \tau c^{*}$) between the critical shear stress of experimental results using CFD modeling and the critical shear stress from Shields' graph using the same CFD modeling. The ration, $\tau c^{*'}/ \tau c^{*}$, for given grain sizes was estimated by calculating the average value of the same particle size. With the calibration of $\tau c^{*'}/ \tau c^{*}$, more reliable estimation of paleowind intensity thresholds were derived (Table 7). 4mm particles' thresholds cannot be modified because there are no measured results of 4mm particles in the wind tunnel. However, wind threshold of D85 is less important than that of D15 or D50, for the reason that the gnamma can still develop when there is a small amount of large particles inside the pit.

Table 6 Critical shear stress ratio between experiments using CFD models and Shields' Diagram.

Re	D	τc* (from gnamma modeling)	τc*' (from Shields' diagram)	τc*'/τc*	τc*'/τc* for D
1.96		0.022	0.092	4.20	
2.13		0.026	0.082	3.17	
2.18	0. 125	0.027	0.082	3.02	3.46
4.52		0.015	0.041	2.81	
4.56		0.015	0.041	2.77	
4.53	0. 25	0.015	0.041	2.81	2.80
11.33		0.011	0.031	2.71	
13.03		0.015	0.031	2.05	
10.80	0. 5	0.010	0.031	2.98	2.58
65.87	2	0.006	0.045	7.44	7.44

Table 7 Modified wind threshold estimation

Pit number	u*/u	D15's u*	D15's u	D50's u*	D50's u	D85's u*	D85's u
M01	0.031	0.38	12.23	0.52	16.73	/	/
M02	0.021	0.38	17.70	0.52	24.22	/	/
M03	0.029	0.38	13.21	0.52	18.08	/	/
M04	0.033	0.38	11.46	0.52	15.69	/	/
S01	0.034	0.38	11.19	0.38	11.19	0.38	11.19
S02	0.039	0.38	9.76	0.38	9.76	0.52	13.35
S04	0.02	0.38	19.41	0.38	19.41	0.38	19.41
S05	0.023	0.38	16.87	0.52	23.08	/	/
S06	0.023	0.38	16.23	0.52	22.20	/	/
S07	0.015	0.38	25.40	0.52	34.76	/	/
S08	0.025	0.38	15.33	0.38	15.33	0.52	20.97
S10	0.032	0.38	11.98	0.52	16.40	/	/

Note: Estimation of 4mm particles cannot be calibrated due to a lack of experiment results.

Chapter 5

CONCLUSION

Gnamma pits provide a link between weathering geomorphology and aeolian geomorphology processes. The growth of weathering pits first requires weathering reduce the grain-to-grain cementation. The detachment of individual grains then allows aeolian processes to operate by deflating grains – thus enlarging the pit. Previously, no research has established the wind speeds needed to enlarge gnamma pits of varying sizes and depths. By using wind tunnel simulation at Arizona State University, I conducted a series of experiments with three pit depths (12mm, 21mm, 45mm) and five grain sizes (4mm, 2mm, 0.5mm, 0.25mm, 0.125mm). The thresholds for these different situations show a positive relationship between wind threshold and grain size and pit depth. In each mold, larger particles require higher speeds to deflate. Also, for a single size particle, deeper molds require more intense wind to deflate particles of the same size. In addition, twenty-four computational fluid dynamics models were run to investigate the distribution of shear stress at the bottom of the pits. With modeled wind velocity and shear stress maximum, multiple regression was used to determine an equation relating the critical shear velocity to wind velocity as a function of depth-to-width ratio. Using this equation with the Shields diagram, the wind threshold can be obtained. However, a comparison of this method with wind tunnel data shows that particles are removed more easily than predicted. This lower experimental threshold of motion may be due to higher turbulent kinetic energy in the bottom pits relative to the Shields diagram developed over flat beds. Fifteen samples were collected from McDowell Mountain and South Mountain, and the velocity thresholds were estimated. Paleowind maximums can be estimated with the aid of experiments, numerical modeling, and fieldwork.

REFERENCES

Cao, Zhixian, Gareth Pender, and Jian Meng. “Explicit Formulation of the Shields Diagram for Incipient Motion of Sediment.” 2006. Journal of Hydraulic Engineering 132 (10): 1097–99. doi:10.1061/(ASCE)0733-9429(2006)132:10(1097).

Cooke, Ronald U., Andrew Warren, and Andrew S. Goudie. 1993. Desert Geomorphology. CRC Press.

Domínguez-Villar, David. 2006. “Early Formation of Gnammas (weathering Pits) in a Recently Glaciated Area of Torres Del Paine, Southern Patagonia (Chile).” Geomorphology 76 (1–2): 137–47. doi:10.1016/j.geomorph.2005.10.006.

Domínguez-Villar, David, Carlos Arteaga, Rosario García-Giménez, Erik A. Smith, and Javier Pedraza. 2008. “Diurnal and Seasonal Water Variations of Temperature, pH, Redox Potential and Conductivity in Gnammas (weathering Pits): Implications for Chemical Weathering.” CATENA 72 (1): 37–48. doi:10.1016/j.catena.2007.03.018.

Domínguez-Villar, David, and Carrie E. Jennings. 2008. “Multi-Phase Evolution of Gnammas (weathering Pits) in a Holocene Deglacial Granite Landscape, Minnesota (USA).” Earth Surface Processes and Landforms 33 (2): 165–77. doi:10.1002/esp.1532.

Dorn, Ronald I. "Rock varnish as an indicator of aeolian environmental change." Aeolian geomorphology (1986): 291-307.

Dorn, Ronald I. 1995. “Digital Processing of Back-Scatter Electron Imagery: A Microscopic Approach to Quantifying Chemical Weathering.” Geological Society of America Bulletin 107 (6): 725. doi:10.1130/0016-7606(1995)107<0725:DPOBSE>2.3.CO;2.

Fahey, Barry D. 1986. “Weathering Pit Development in the Central Otago Mountains of Southern New Zealand.” Arctic and Alpine Research 18 (3): 337. doi:10.2307/1550891.

Goudie, Andrew S. 2007. “Mega-Yardangs: A Global Analysis.” Geography Compass 1 (1): 65–81. doi:10.1111/j.1749-8198.2006.00003.x.

Grass, A. J. 1971. “Structural Features of Turbulent Flow over Smooth and Rough Boundaries.” Journal of Fluid Mechanics 50 (02): 233–55. doi:10.1017/S0022112071002556.

Greeley, R., J. D. Iversen, J. B. Pollack, Nancy Udovich, and B. White. 1974. “Wind Tunnel Studies of Martian Aeolian Processes.” Proceedings of the Royal Society of London. A. Mathematical and Physical Sciences 341 (1626): 331–60. doi:10.1098/rspa.1974.0191.

Gutiérrez-Elorza, M, G Desir, and F Gutiérrez-Santolalla. 2002. “Yardangs in the Semiarid Central Sector of the Ebro Depression (NE Spain).” Geomorphology 44 (1–2): 155–70. doi:10.1016/S0169-555X(01)00151-9.

Hall, Adrian Malcom, and William Morton Phillips. 2006. “Weathering Pits as Indicators of the Relative Age of Granite Surfaces in the Cairngorm Mountains, Scotland.” Geografiska Annaler: Series A, Physical Geography 88 (2): 135–50. doi:10.1111/j.0435-3676.2006.00290.x.

Hesp, Patrick A., and Robert Hyde. 1996. “Flow Dynamics and Geomorphology of a Trough Blowout.” Sedimentology 43 (3): 505–25. doi:10.1046/j.1365-3091.1996.d01-22.x.

Holcombe, Troy Leon, Trevor Ley, and Dale A. Gillette. 1997. “Effects of Prior Precipitation and Source Area Characteristics on Threshold Wind Velocities for Blowing Dust Episodes, Sonoran Desert 1948–78.” Journal of Applied Meteorology 36 (9): 1160–75. doi:10.1175/1520-0450(1997)036<1160:EOPPAS>2.0.CO;2.

Jackson, D. W. T., J. H. M. Beyers, K. Lynch, J. a. G. Cooper, A. C. W. Baas, and I. Delgado-Fernandez. 2011. “Investigation of Three-Dimensional Wind Flow Behaviour over Coastal Dune Morphology under Offshore Winds Using Computational Fluid Dynamics (CFD) and Ultrasonic Anemometry.” Earth Surface Processes and Landforms 36 (8): 1113–24. doi:10.1002/esp.2139.

Kirkby, Michael J. 1971. “Hillslope process-response models based on the continuity equation.” Special Publication Institute British Geographers, 3, 15-30.

Laity, Julie E. 1987. “Topographic Effects on Ventifact Development, Mojave Desert, California.” Physical Geography 8 (2): 113–32. doi:10.1080/02723646.1987.10642315.

Laity, Julie E. 2009. “Landforms, Landscapes, and Processes of Aeolian Erosion.” In Geomorphology of Desert Environments, edited by Dr Anthony J. Parsons and Athol D. Abrahams, 597–627. Springer Netherlands. http://link.springer.com/chapter/10.1007/978-1-4020-5719-9_19.

Miller, M. C., I. N. McCAVE, and P. D. Komar. 1977. “Threshold of Sediment Motion under Unidirectional Currents.” Sedimentology 24 (4): 507–27. doi:10.1111/j.1365-3091.1977.tb00136.x.

Netoff, Dennis I., and Marjorie A. Chan. 2009. “Aeolian Activity at a Giant Sandstone Weathering Pit in Arid South-Central Utah.” Earth Surface Processes and Landforms 34 (1): 99–108. doi:10.1002/esp.1697.

Parsons, Daniel R., Giles F. S. Wiggs, Ian J. Walker, Robert I. Ferguson, and Brian G. Garvey. 2004. “Numerical Modelling of Airflow over an Idealised Transverse Dune.” Environmental Modelling & Software 19 (2): 153–62. doi:10.1016/S1364-8152(03)00117-8.

Sebe, Krisztina, Gábor Csillag, Zsófia Ruszkiczay-Rüdiger, László Fodor, Edit Thamó-Bozsó, Pál Müller, and Régis Braucher. 2011. “Wind Erosion under Cold Climate: A Pleistocene Periglacial Mega-Yardang System in Central Europe (Western Pannonian Basin, Hungary).” Geomorphology 134 (3–4): 470–82. doi:10.1016/j.geomorph.2011.08.003.

Shields, Albert. Application of similarity principles and turbulence research to bed-load movement. Soil Conservation Service, 1936.

Smith, B. J. 2009. “Weathering Processes and Forms.” In Geomorphology of Desert Environments, edited by Dr Anthony J. Parsons and Athol D. Abrahams, 69–100. Springer Netherlands. http://link.springer.com/chapter/10.1007/978-1-4020-5719-9_4.

Stout, John E. 1998. “Effect of Averaging Time on the Apparent Threshold for Aeolian Transport.” Journal of Arid Environments 39 (3): 395–401. doi:10.1006/jare.1997.0370.

Tian, Fei, Mingzhong Tian, and Jin Liu. 2013. “Characteristics, Multi-Phase Evolution and Genesis of Weathering Pits in Qing Mountain, Inner Mongolia, China.” Journal of Earth Science 24 (3): 457–70. doi:10.1007/s12583-013-0336-z.

Twidale, C. R. 1965. “Weather Pit (Gnamma).” Australian Geographer 9 (5): 318–19. doi:10.1080/00049186508702442.

Walker, Ian J., and William G. Nickling. 2002. “Dynamics of Secondary Airflow and Sediment Transport over and in the Lee of Transverse Dunes.” Progress in Physical Geography 26 (1): 47–75. doi:10.1191/0309133302pp325ra.

Ward, A. W., and Ronald Greeley. 1984. “Evolution of the Yardangs at Rogers Lake, California.” Geological Society of America Bulletin 95 (7): 829–37. doi:10.1130/0016-7606(1984)95<829:EOTYAR>2.0.CO;2.

Webb, Nicholas P., and Hamish A. McGowan. 2009. “Approaches to Modelling Land Erodibility by Wind.” Progress in Physical Geography 33 (5): 587–613. doi:10.1177/0309133309341604.

Yakhot, V., S. A. Orszag, S. Thangam, T. B. Gatski, and C. G. Speziale. 1992. “Development of Turbulence Models for Shear Flows by a Double Expansion Technique.” Physics of Fluids A: Fluid Dynamics (1989-1993) 4 (7): 1510–20. doi:10.1063/1.858424.

APPENDIX A

COMPUTATIONAL FLUID DYNAMICS MODELING RESULTS

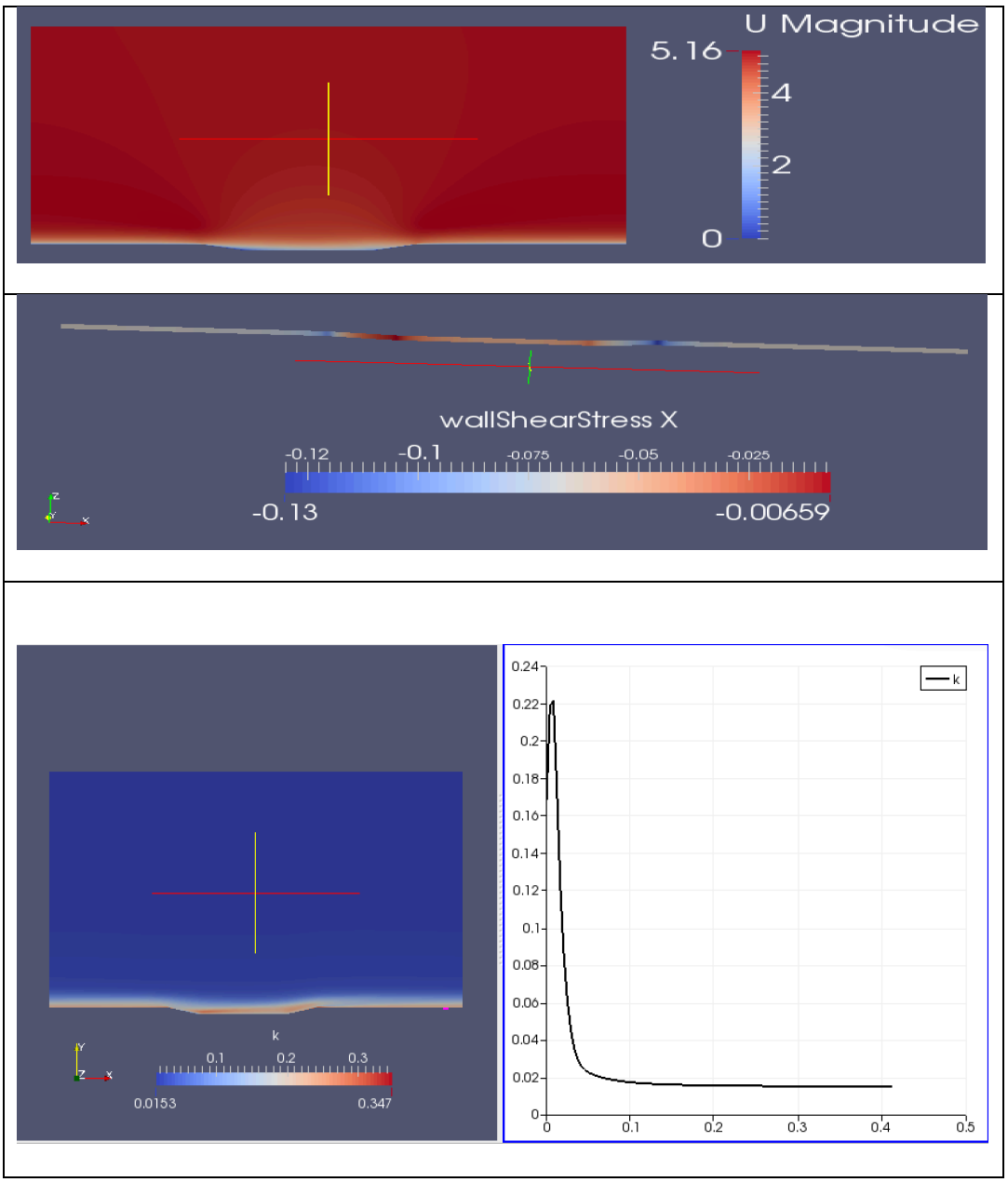

Velocity, shear stress, and turbulent kinetic energy of 5m/s wind flow over 12mm pit

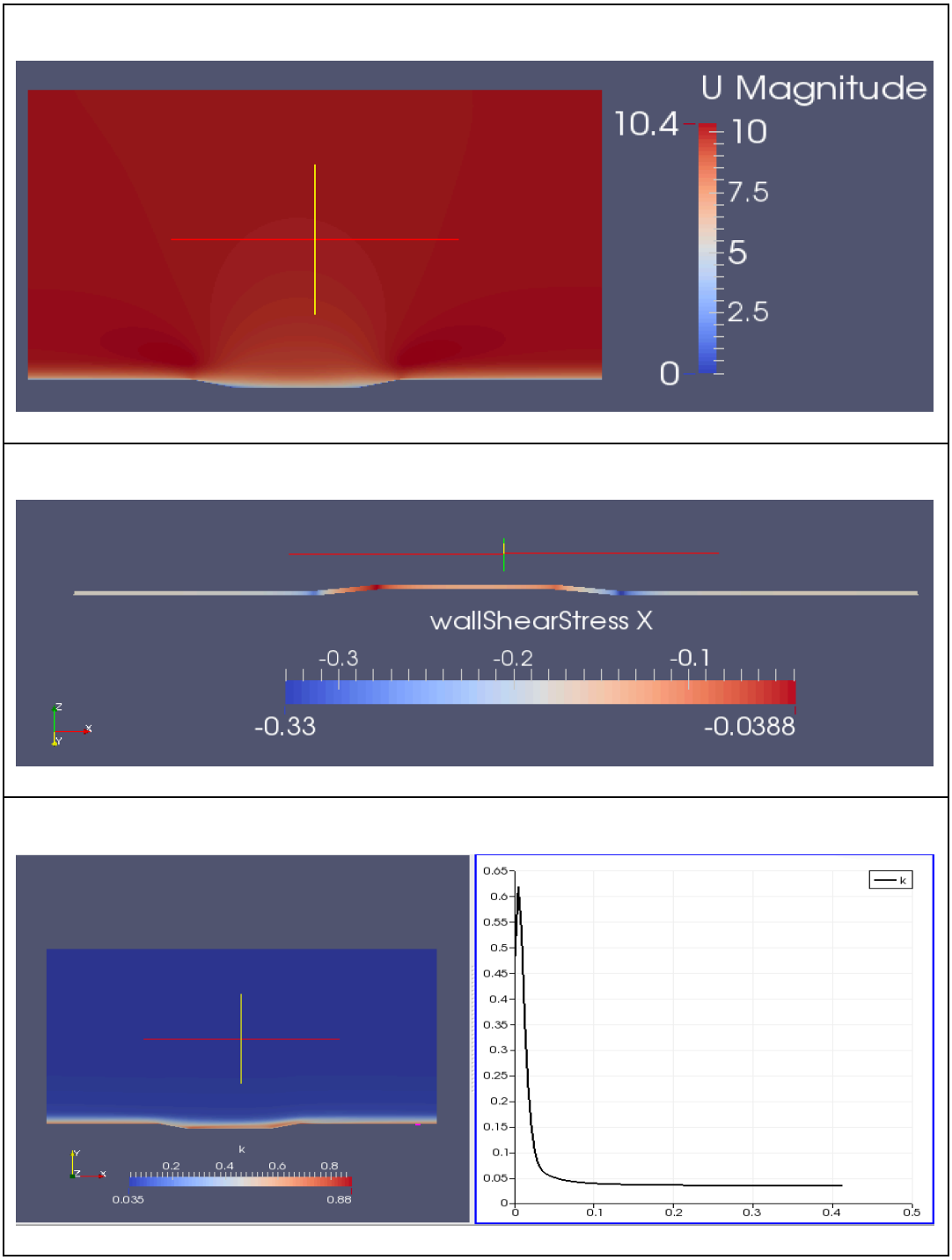

Velocity, shear stress, and turbulent kinetic energy of 10m/s wind flow over 12mm pit

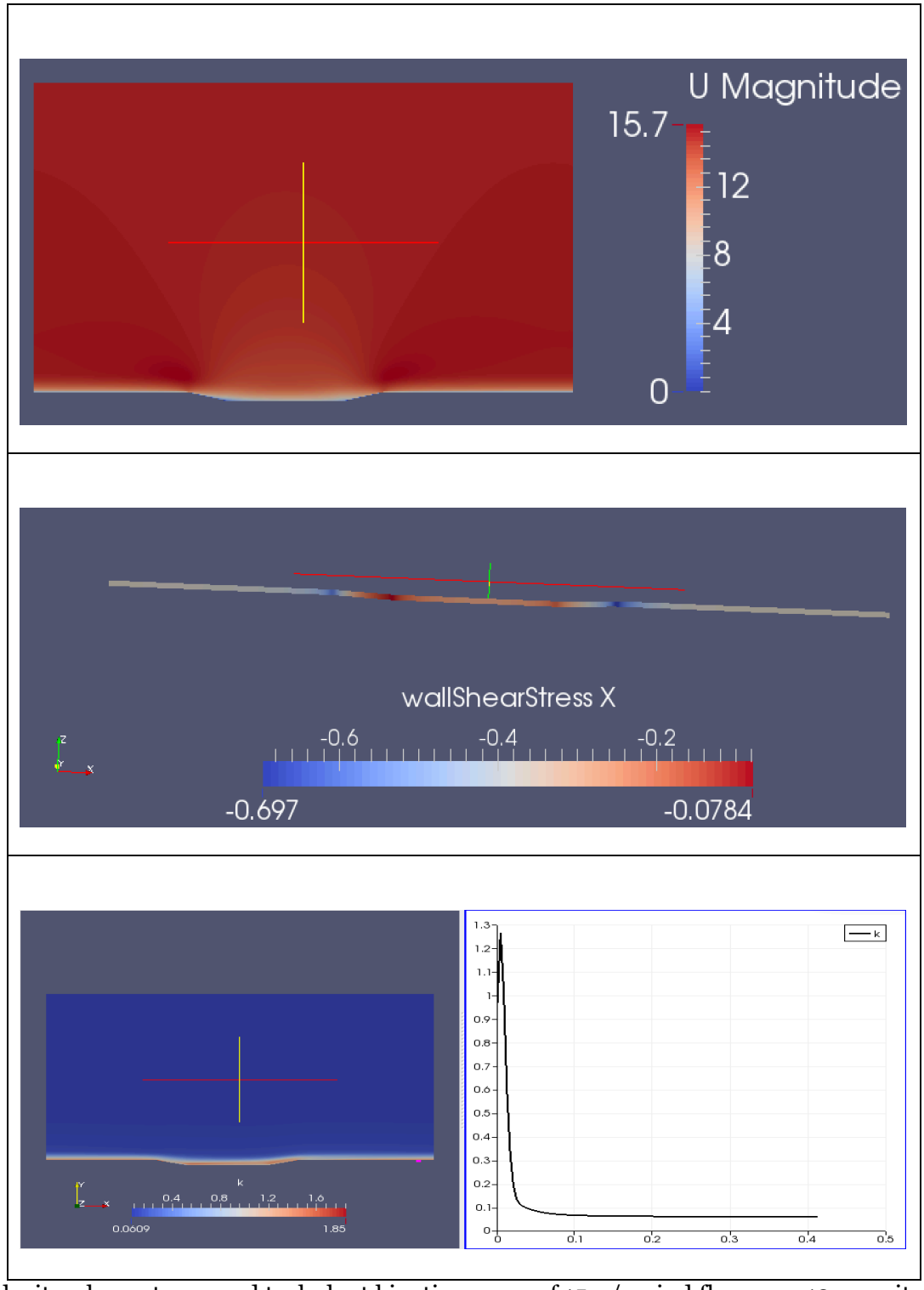

Velocity, shear stress, and turbulent kinetic energy of 15m/s wind flow over 12mm pit

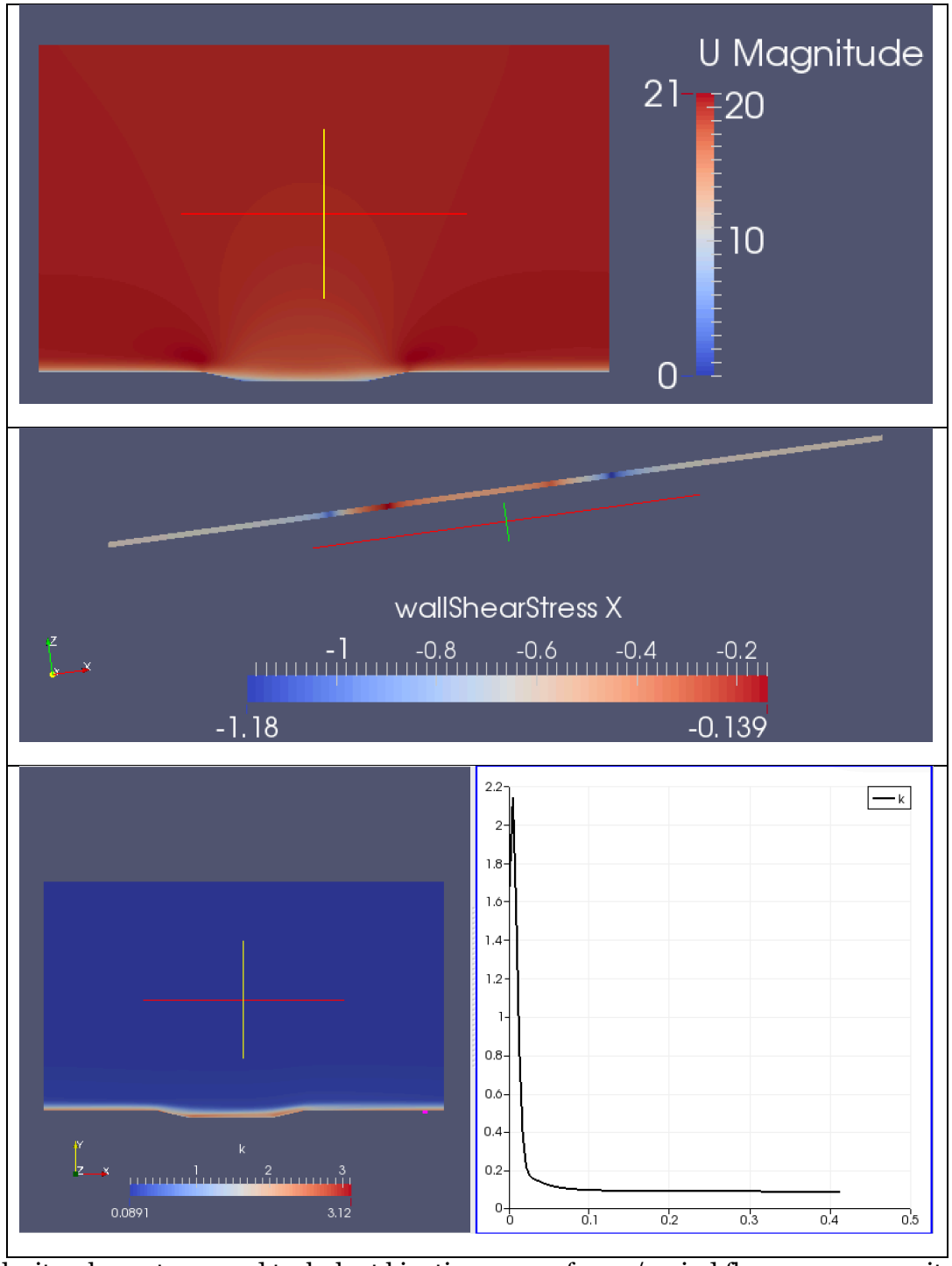

Velocity, shear stress, and turbulent kinetic energy of 20m/s wind flow over 12mm pit

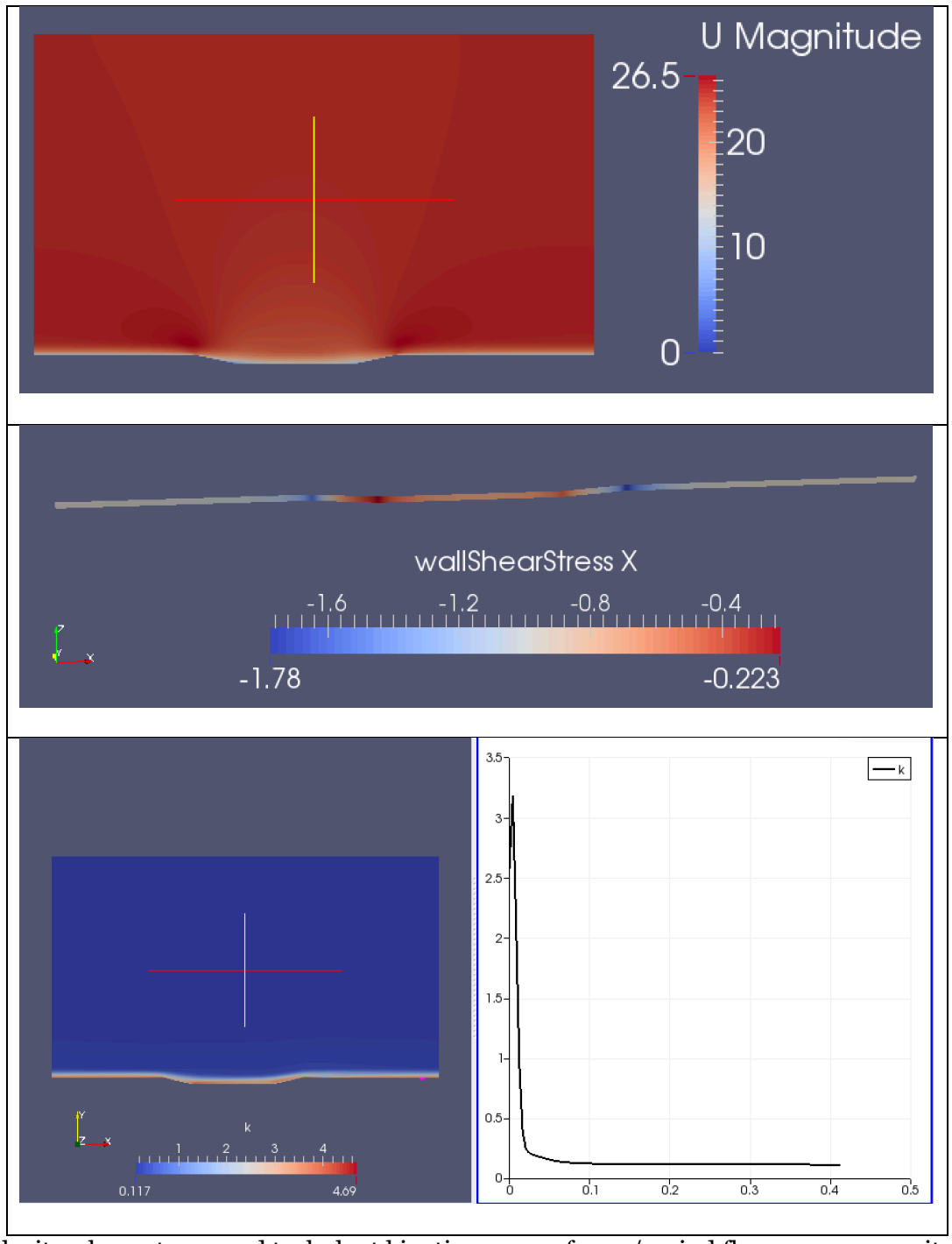

Velocity, shear stress, and turbulent kinetic energy of 25m/s wind flow over 12mm pit

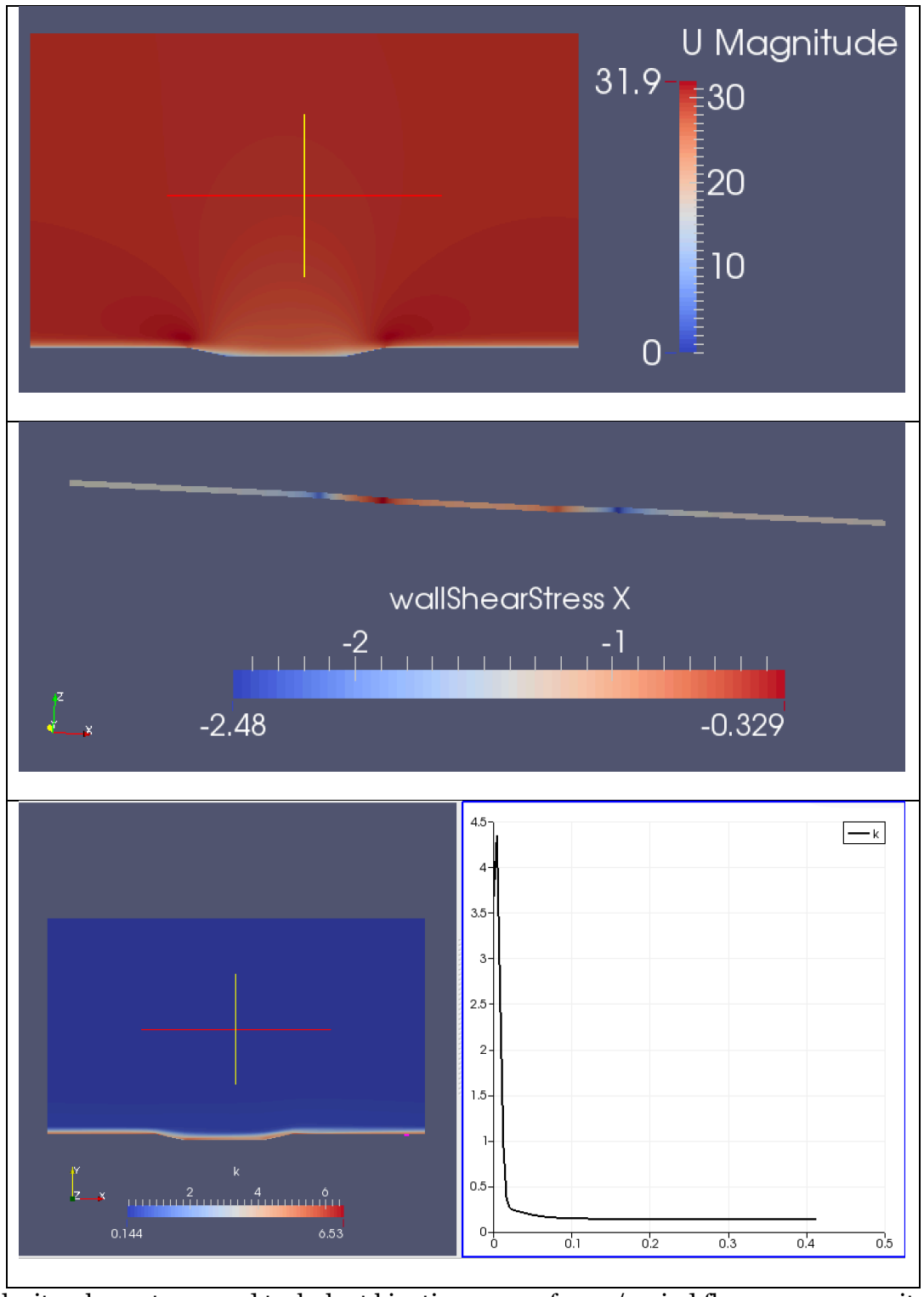

Velocity, shear stress, and turbulent kinetic energy of 30m/s wind flow over 12mm pit

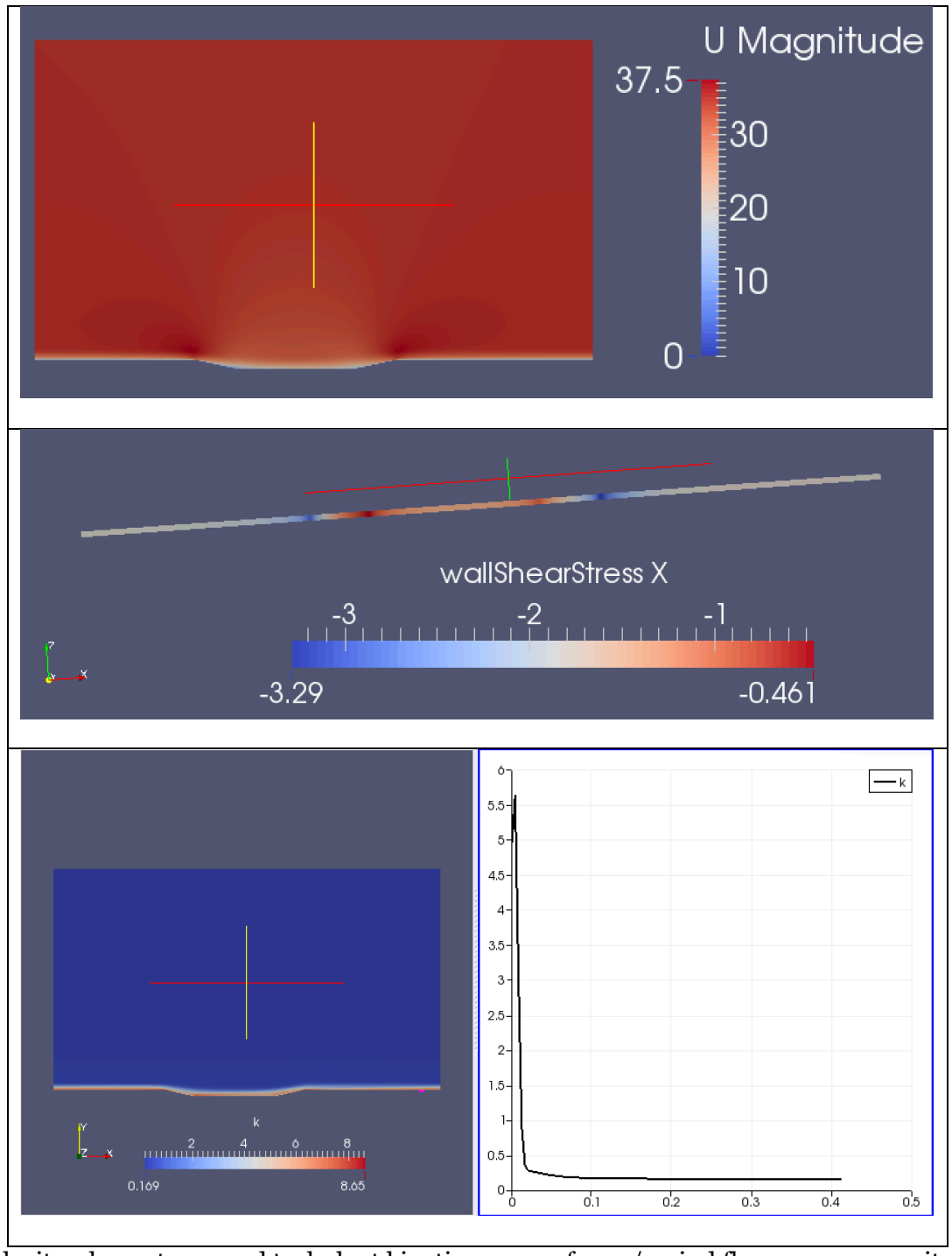

Velocity, shear stress, and turbulent kinetic energy of 35m/s wind flow over 12mm pit

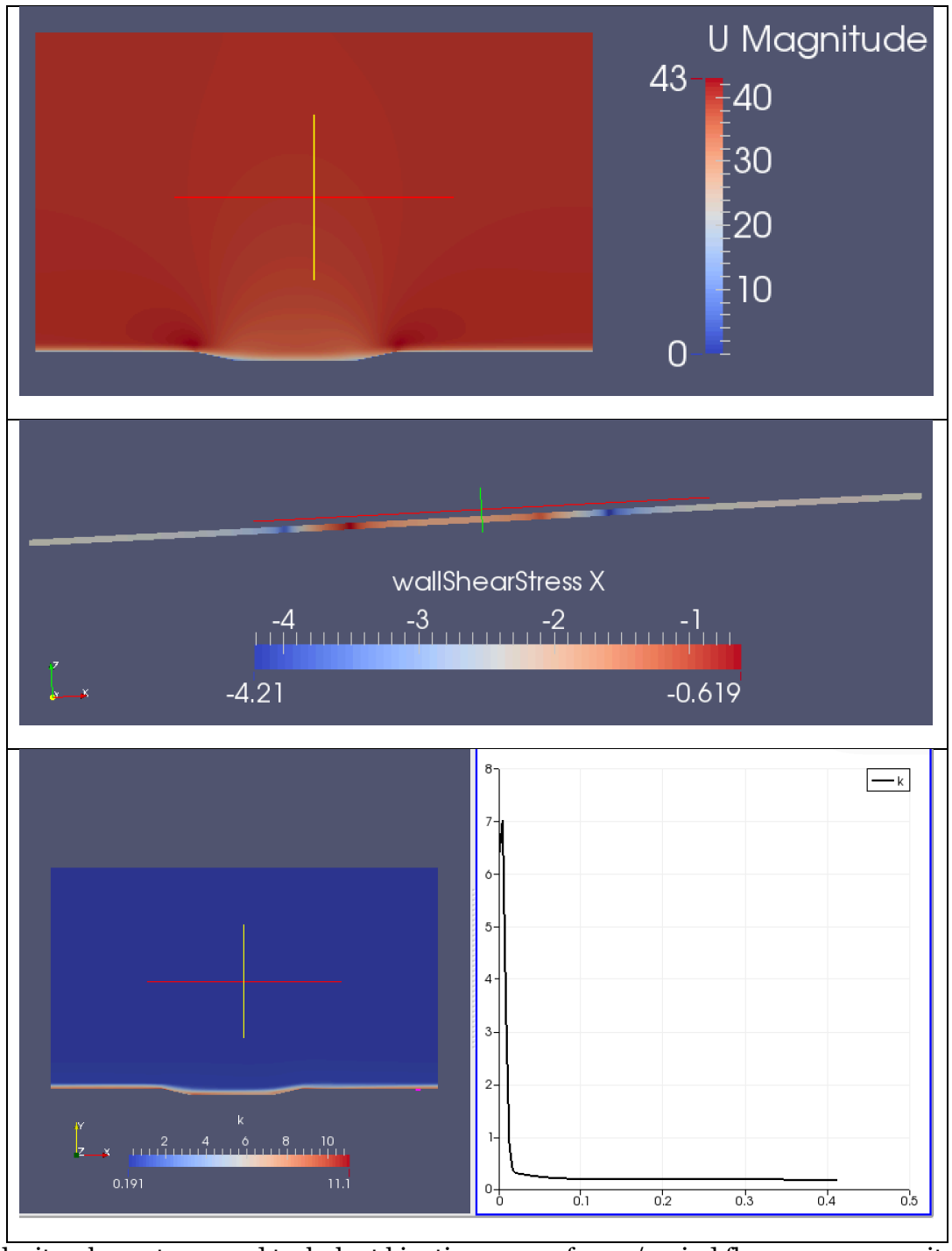

Velocity, shear stress, and turbulent kinetic energy of 40m/s wind flow over 12mm pit

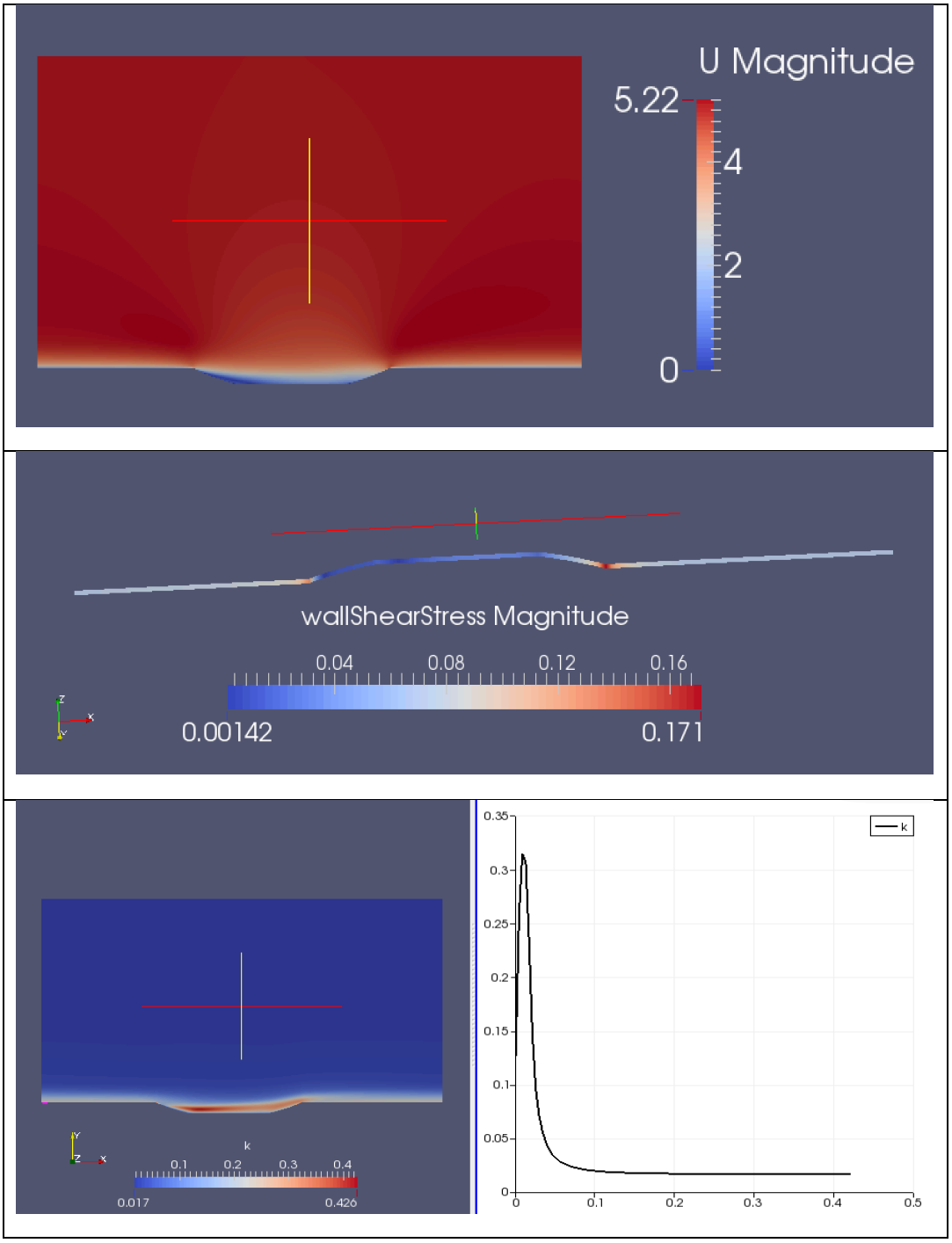

Velocity, shear stress, and turbulent kinetic energy of 5m/s wind flow over 21mm pit

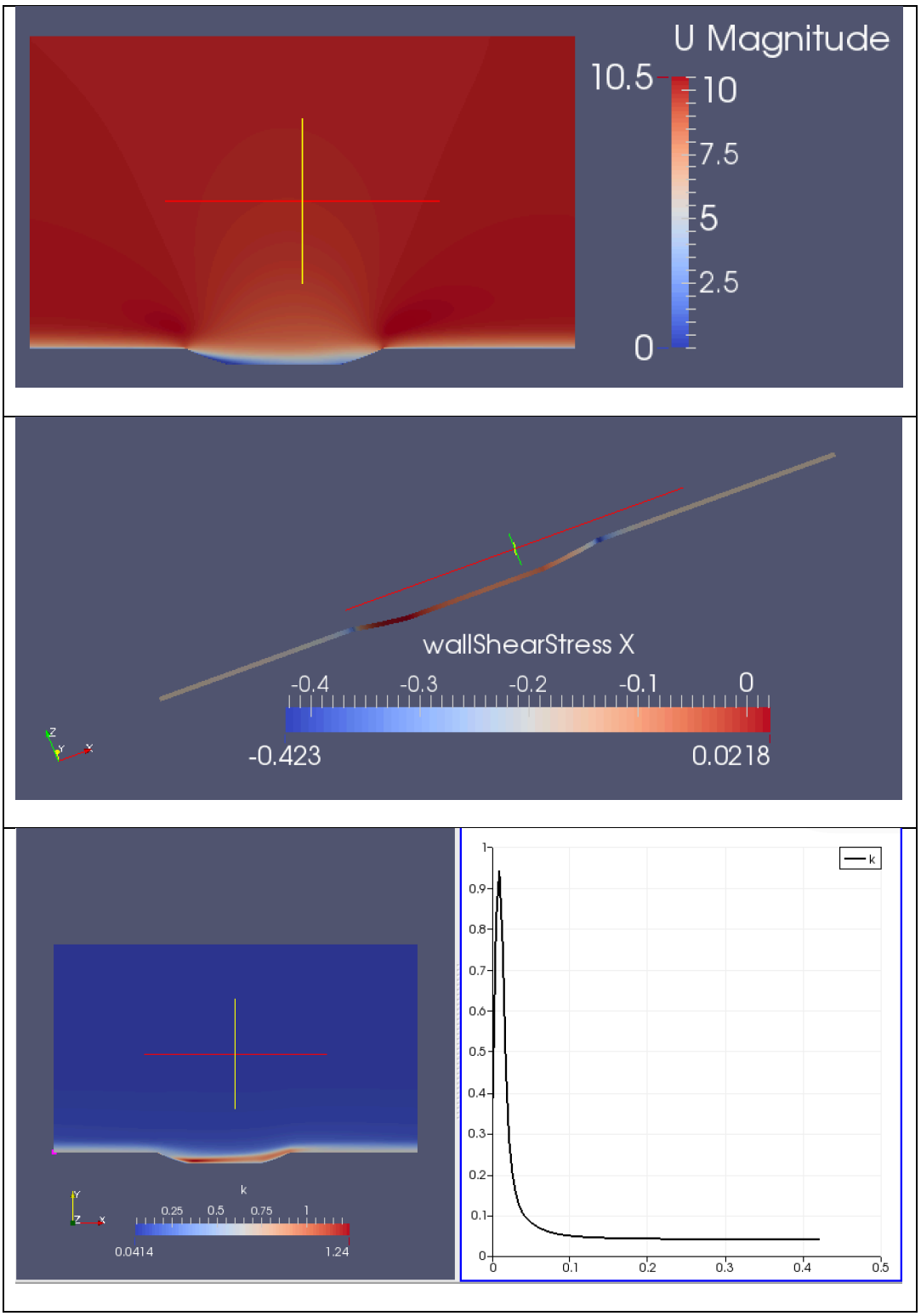

Velocity, shear stress, and turbulent kinetic energy of 10m/s wind flow over 21mm pit

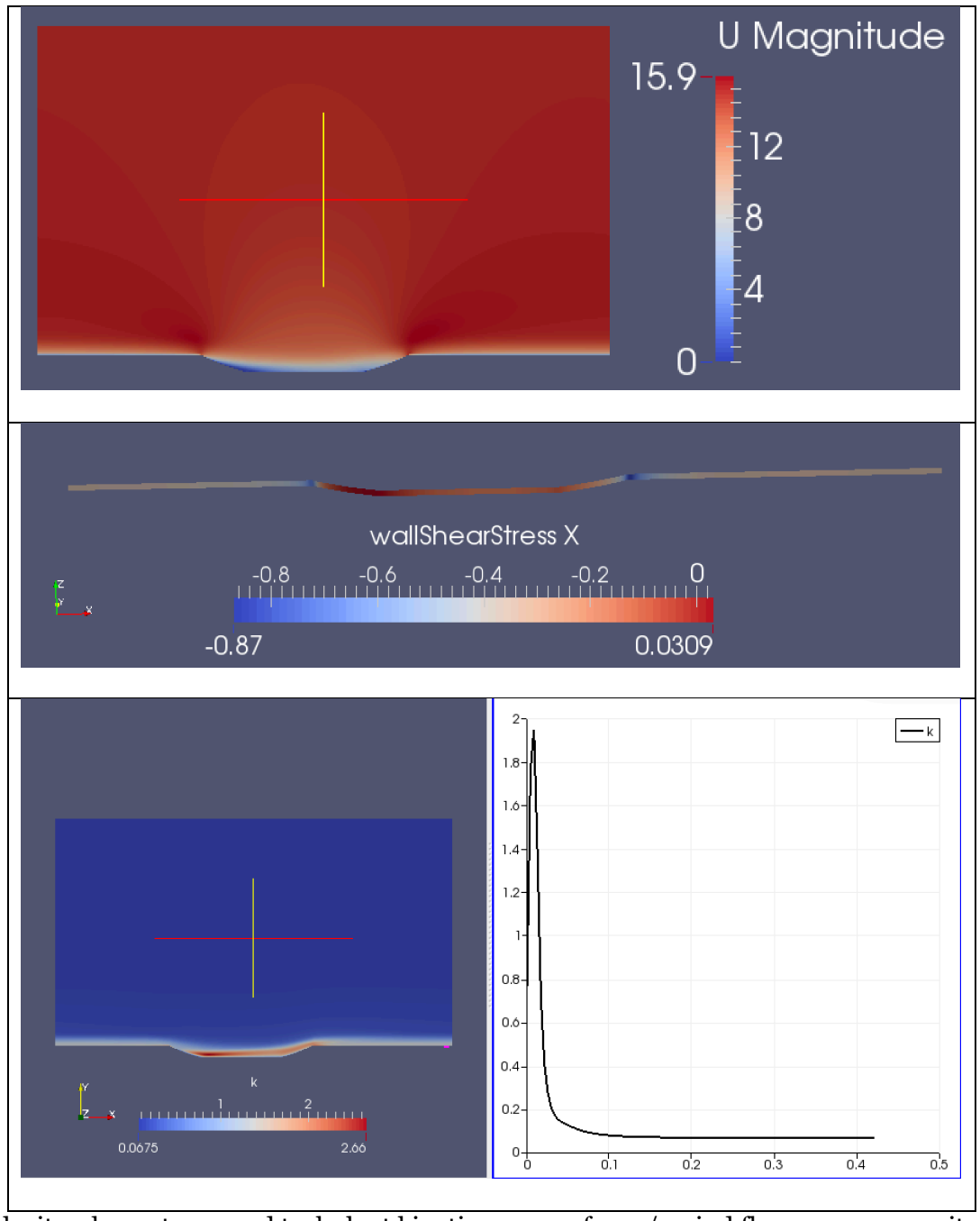

Velocity, shear stress, and turbulent kinetic energy of 15m/s wind flow over 21mm pit

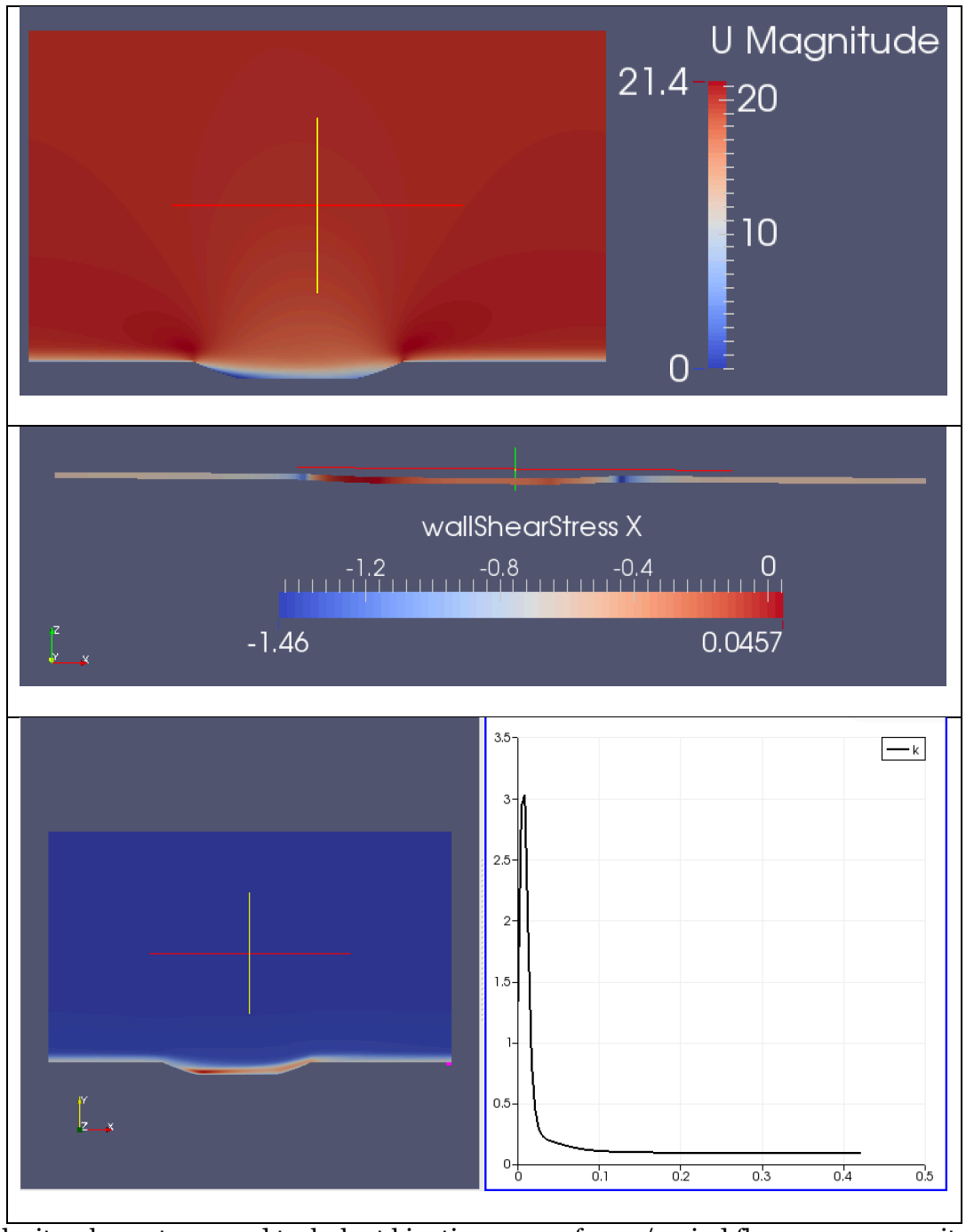

Velocity, shear stress, and turbulent kinetic energy of 20m/s wind flow over 21mm pit

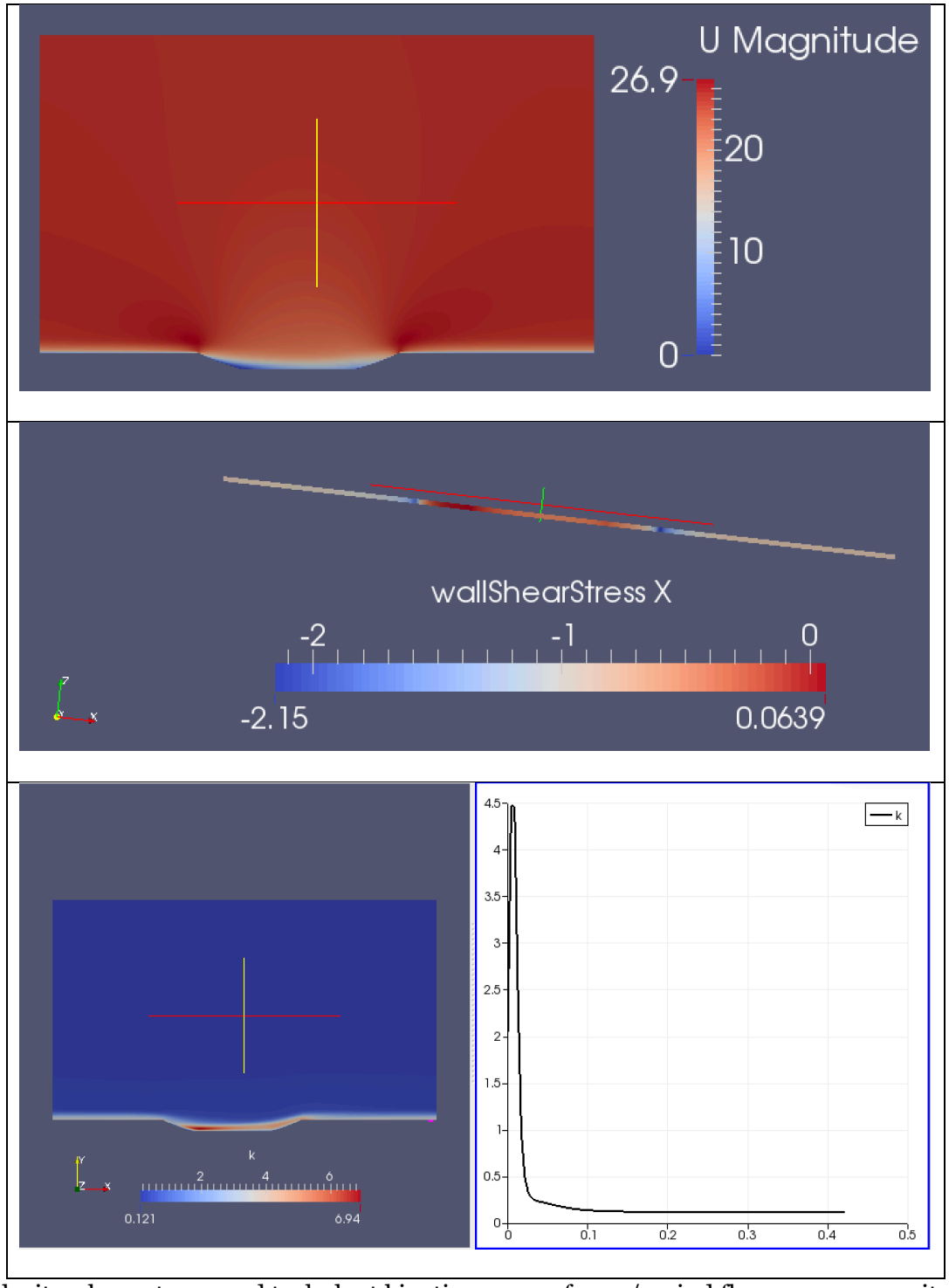

Velocity, shear stress, and turbulent kinetic energy of 25m/s wind flow over 21mm pit

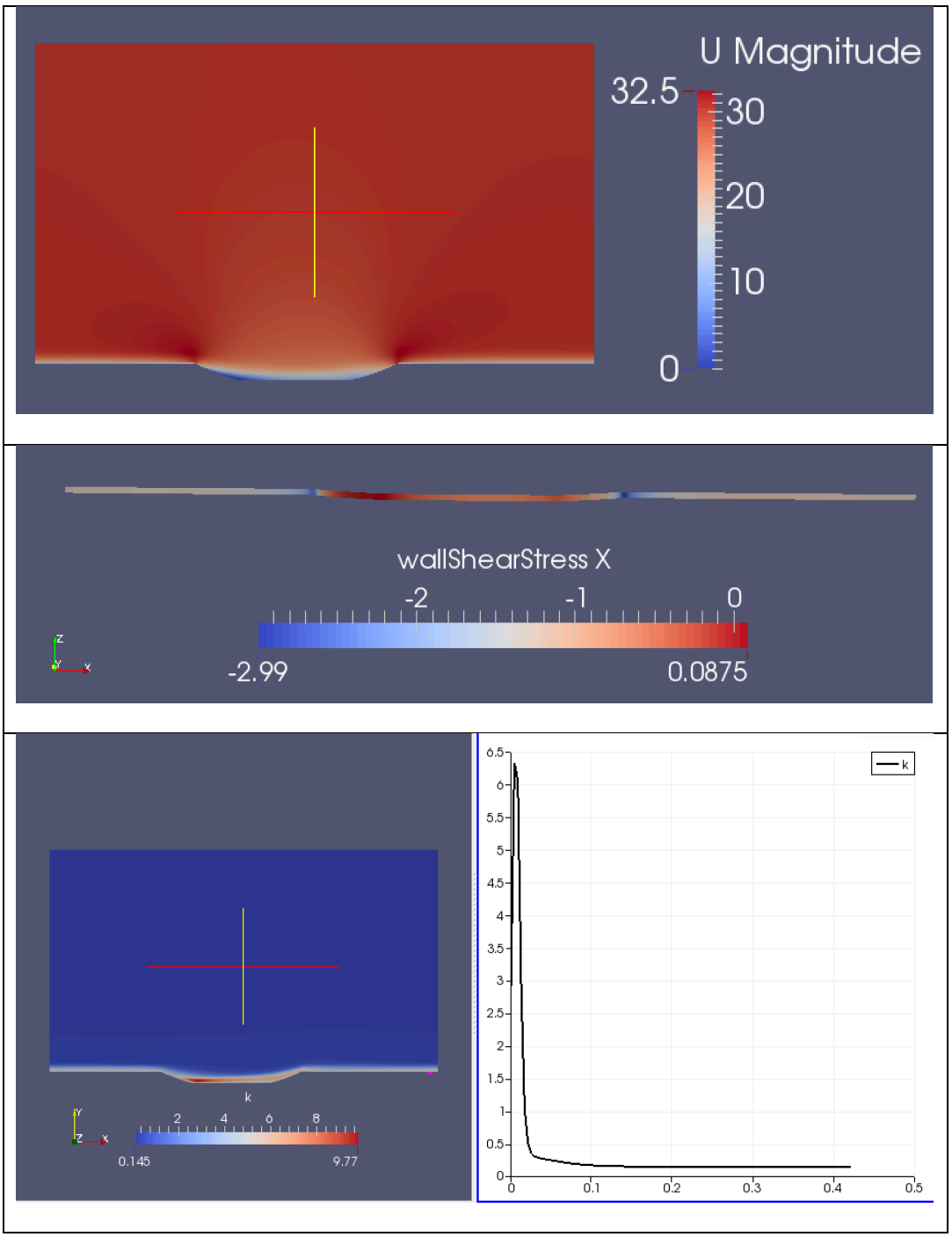

Velocity, shear stress, and turbulent kinetic energy of 30m/s wind flow over 21mm pit

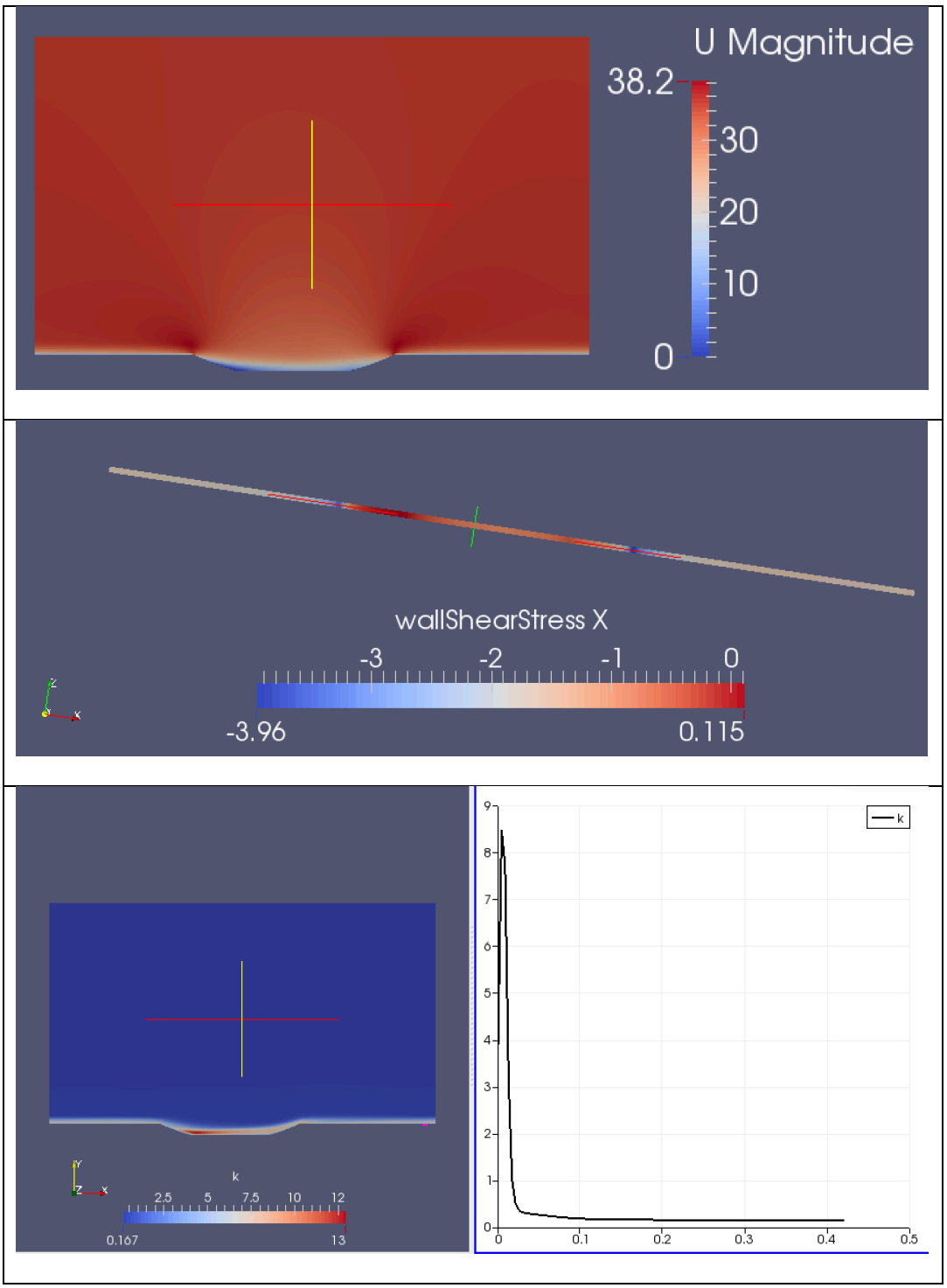

Velocity, shear stress, and turbulent kinetic energy of 35m/s wind flow over 21mm pit

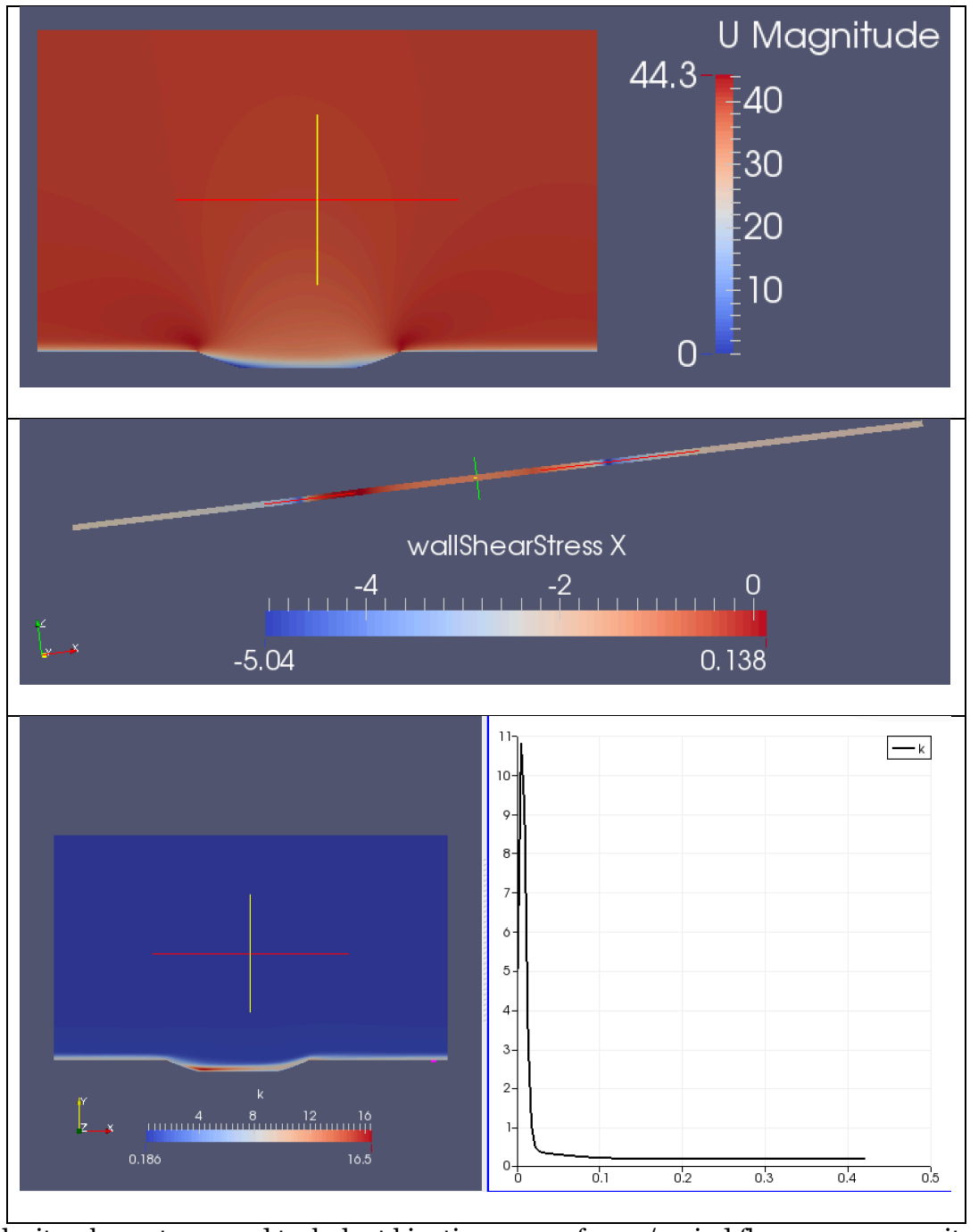

Velocity, shear stress, and turbulent kinetic energy of 40m/s wind flow over 21mm pit

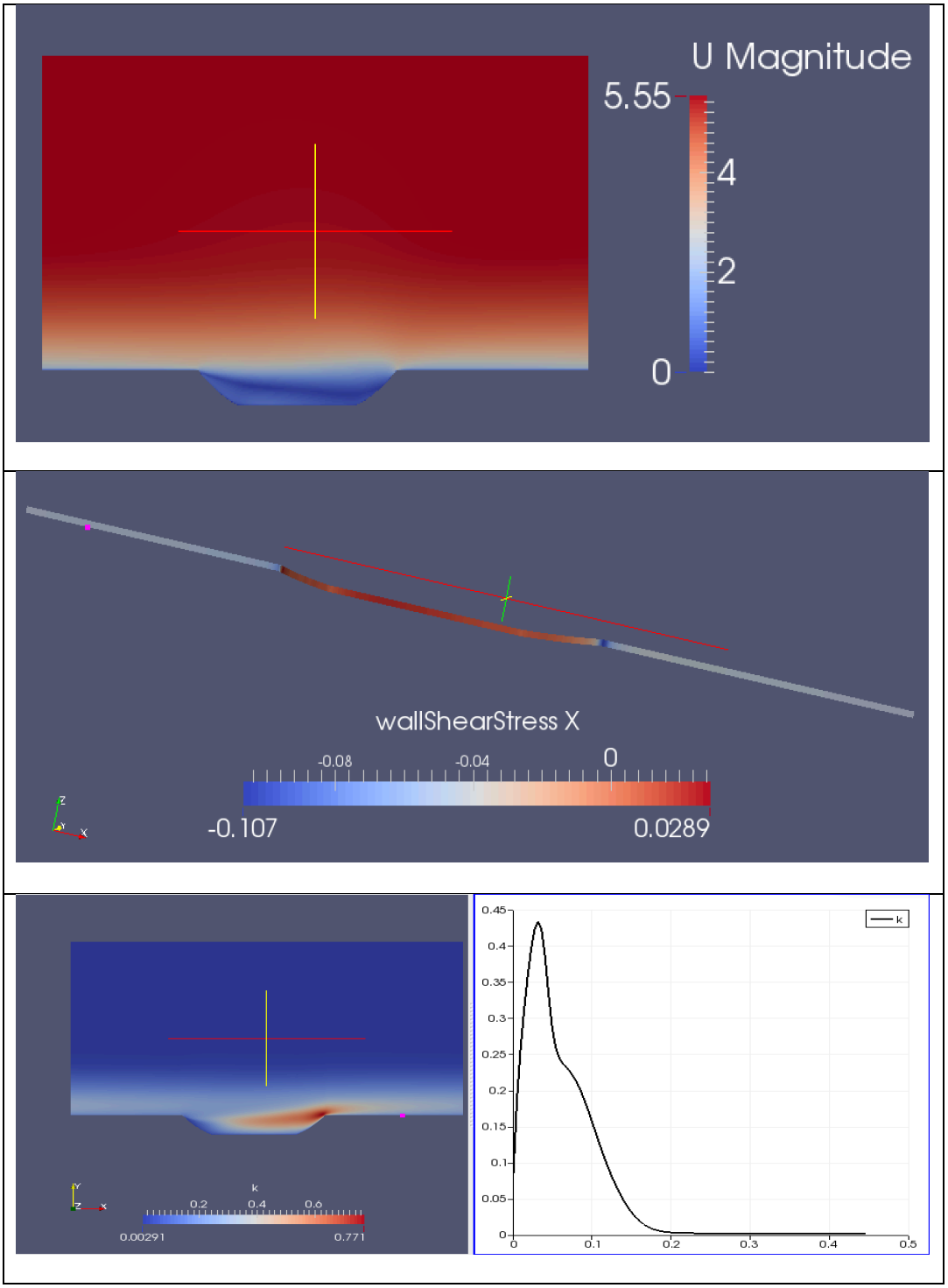

Velocity, shear stress, and turbulent kinetic energy of 5m/s wind flow over 45mm pit

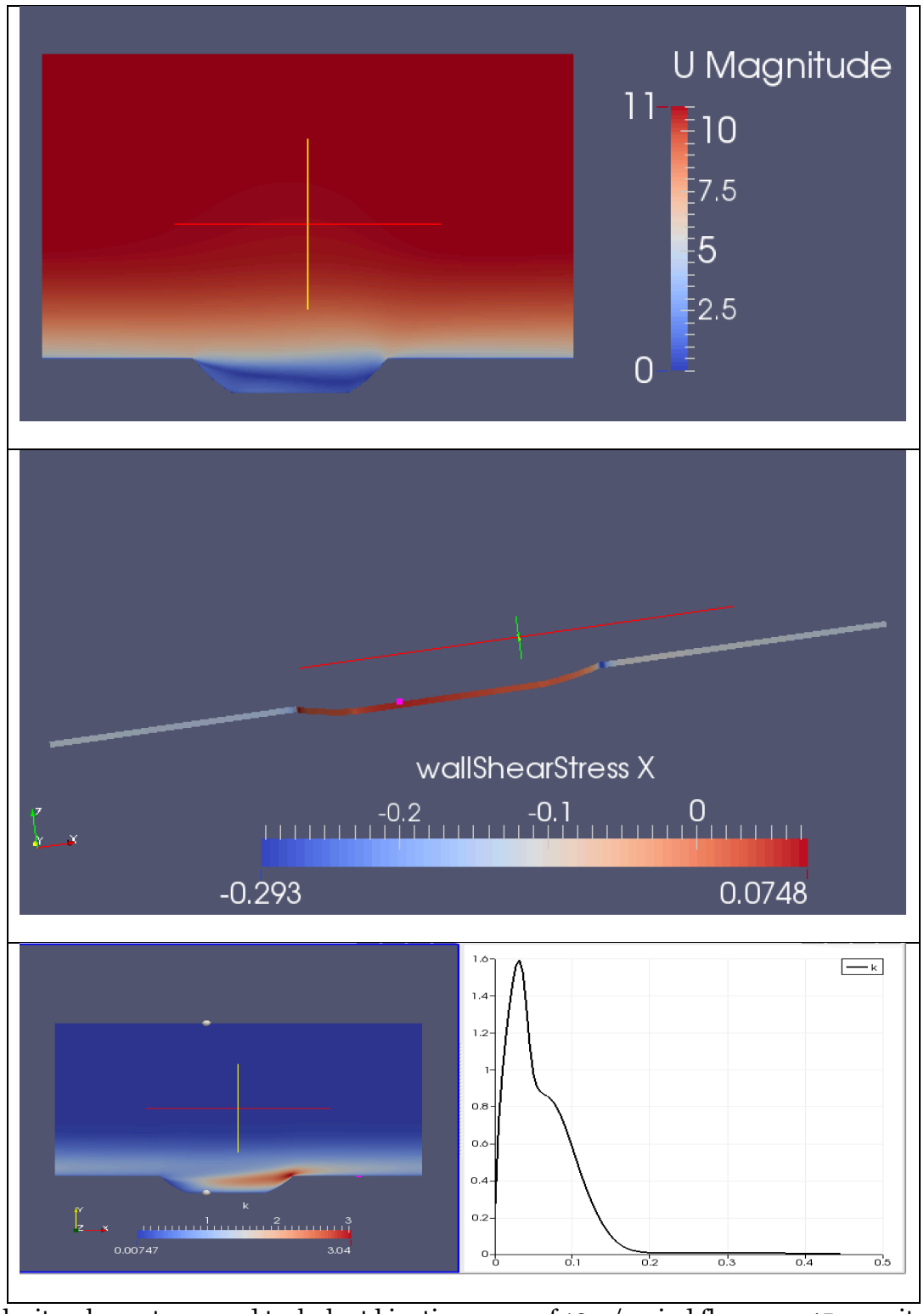

Velocity, shear stress, and turbulent kinetic energy of 10m/s wind flow over 45mm pit

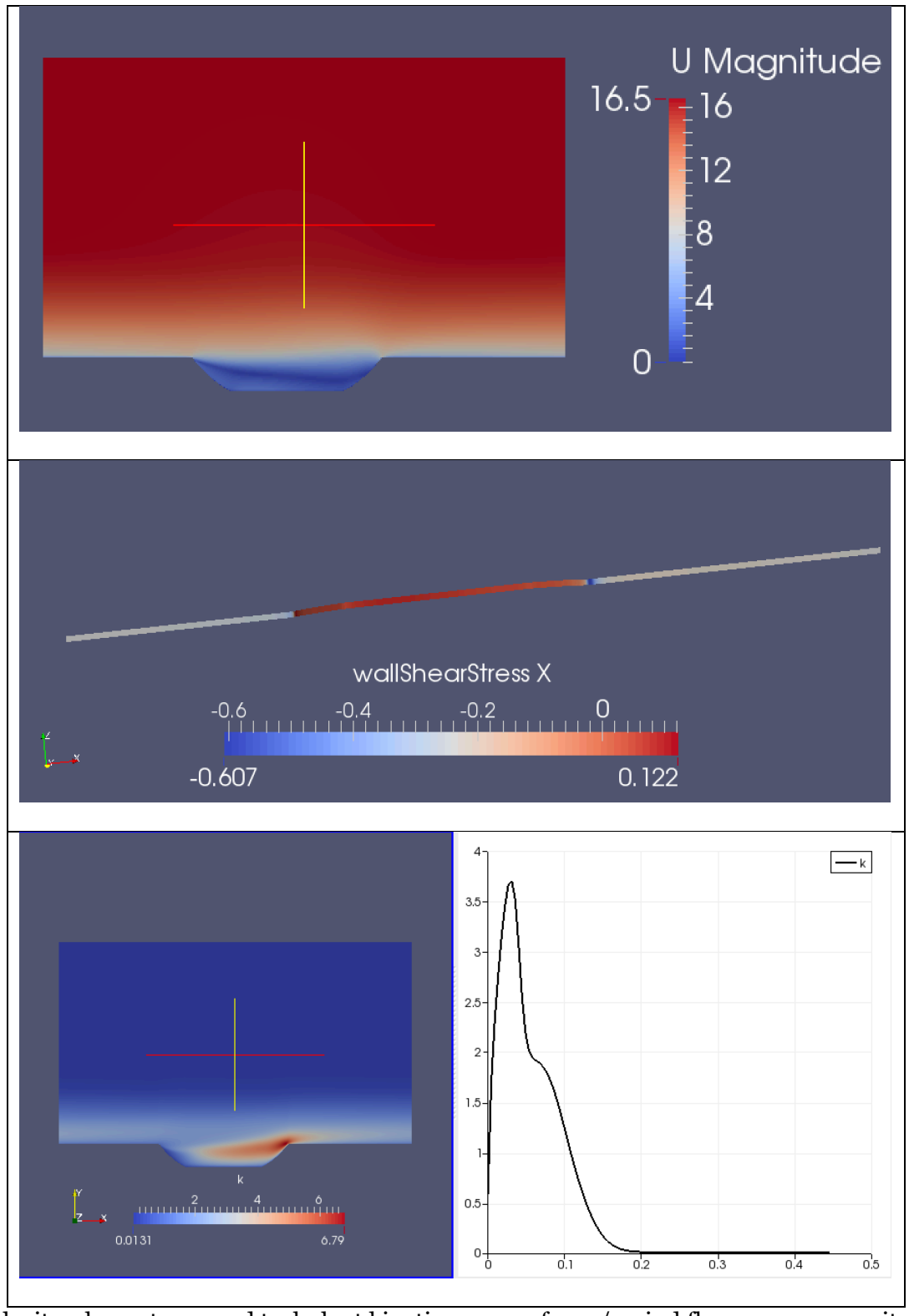

Velocity, shear stress, and turbulent kinetic energy of 15m/s wind flow over 45mm pit

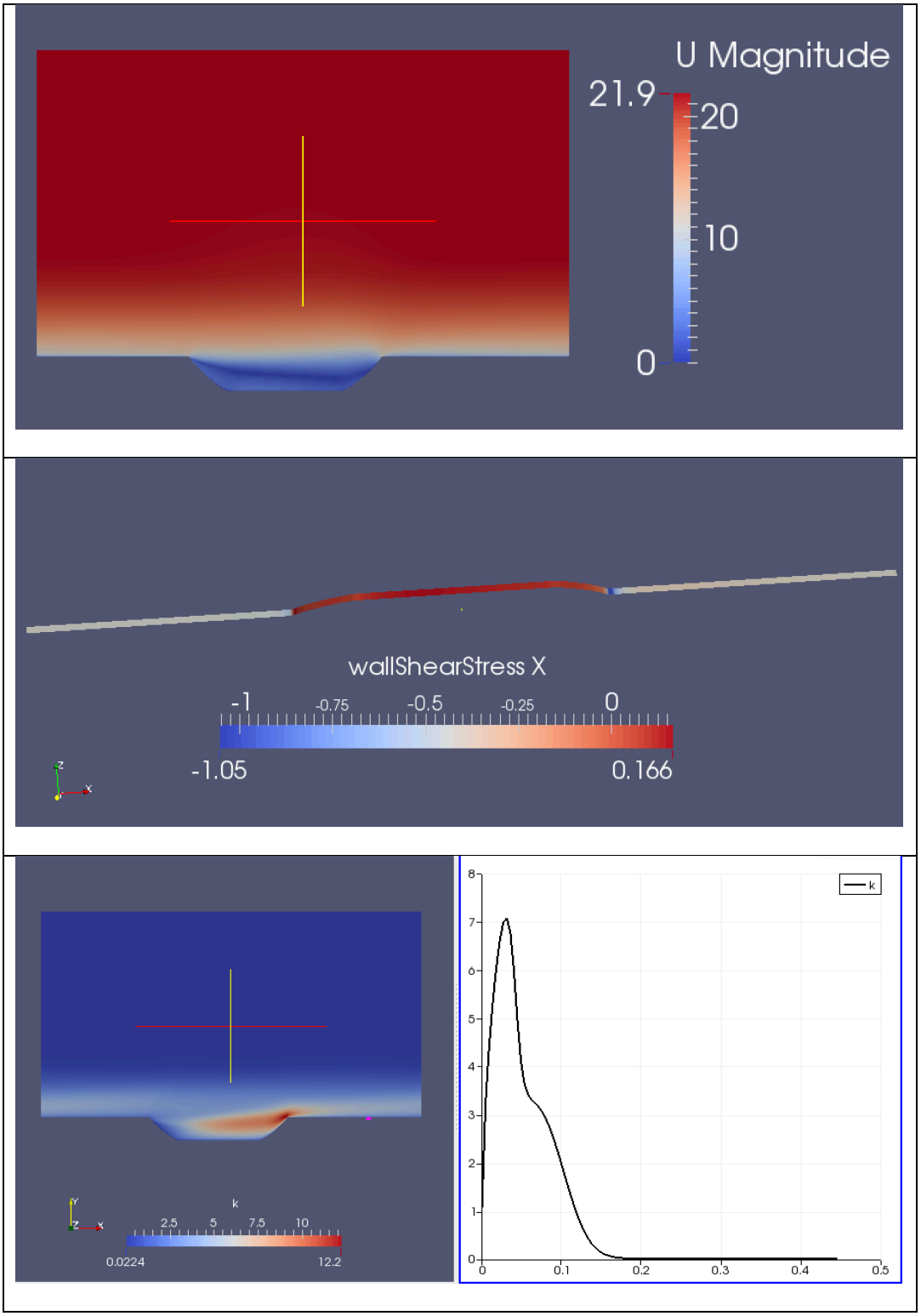

Velocity, shear stress, and turbulent kinetic energy of 20m/s wind flow over 45mm pit

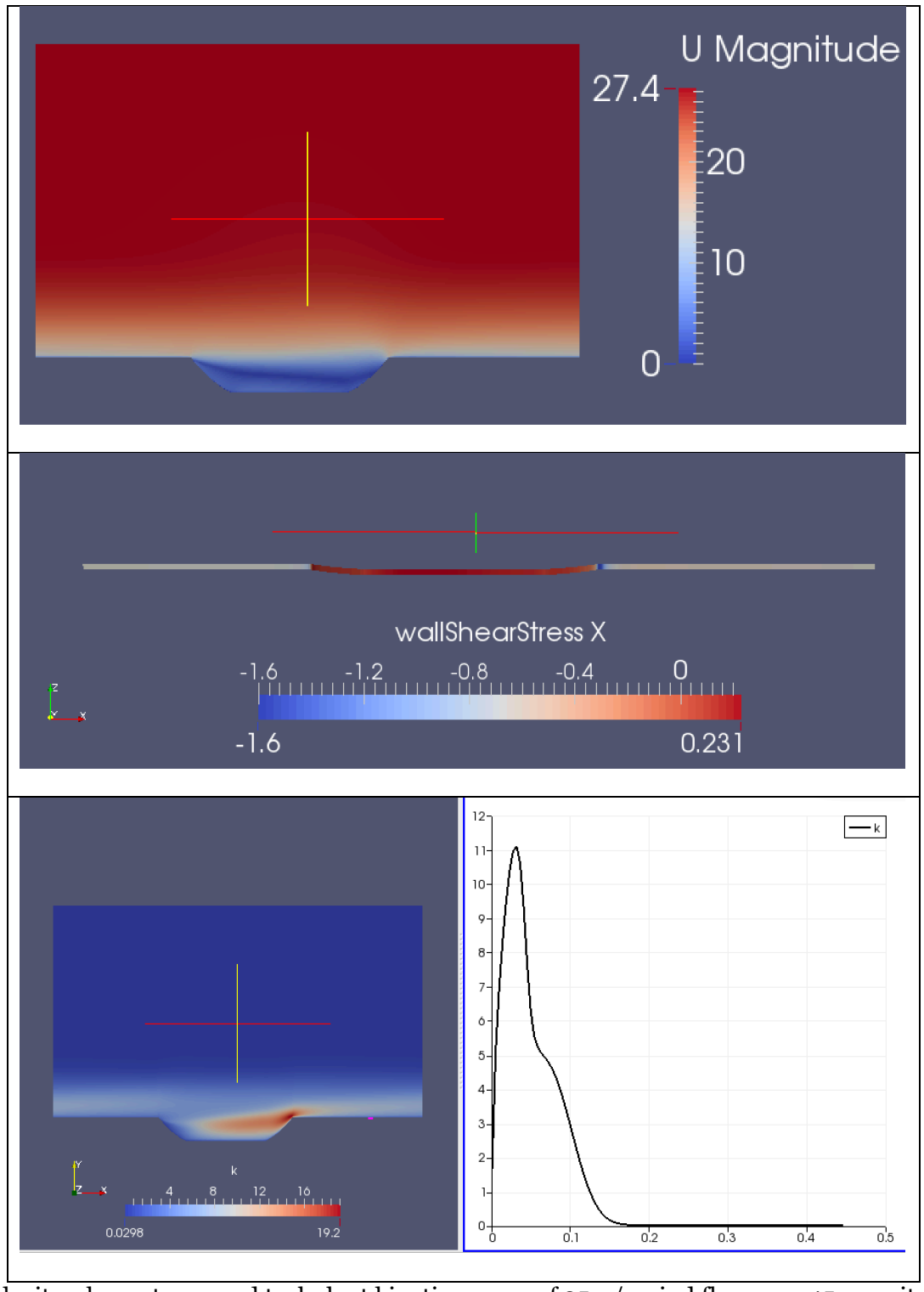

Velocity, shear stress, and turbulent kinetic energy of 25m/s wind flow over 45mm pit

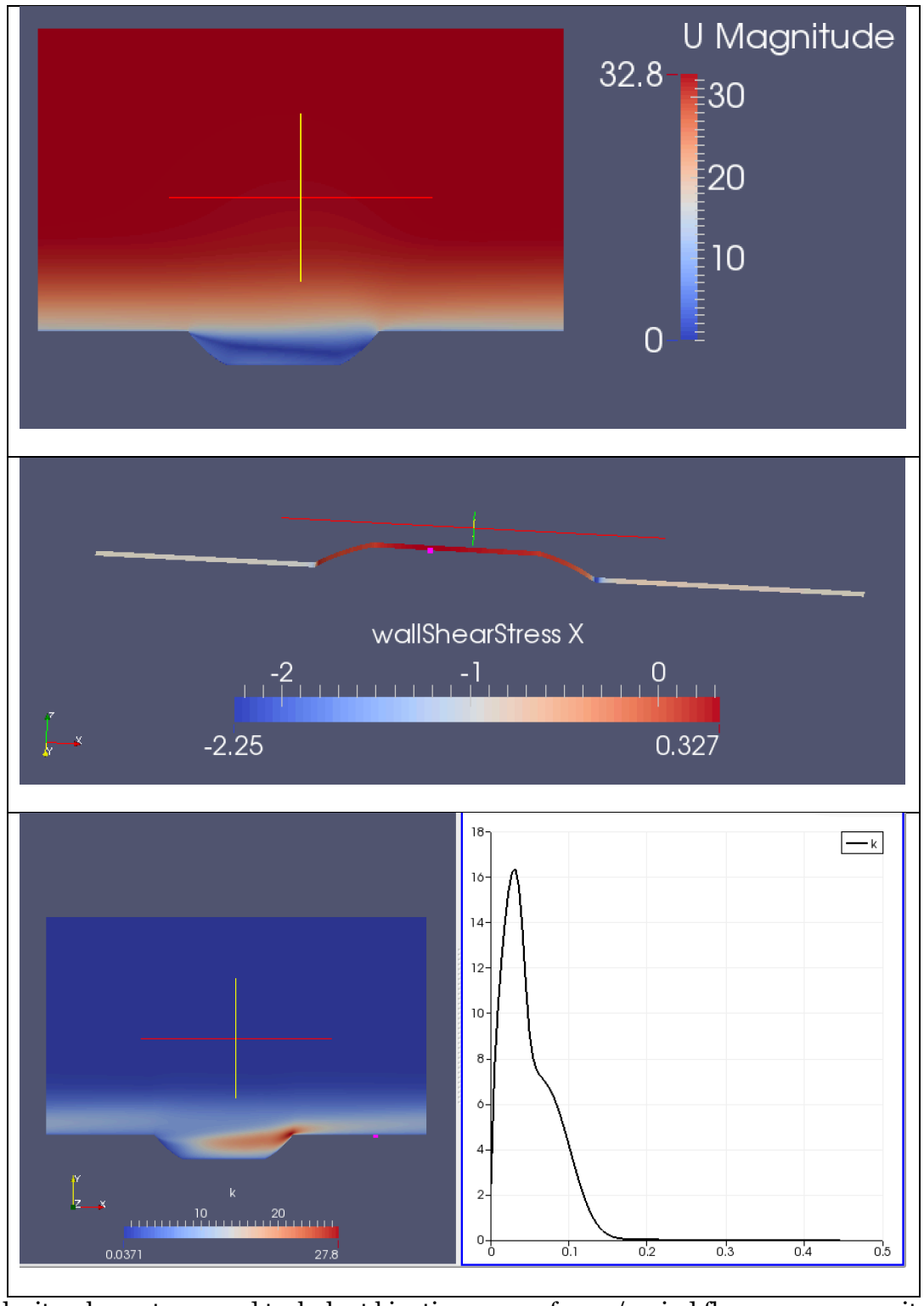

Velocity, shear stress, and turbulent kinetic energy of 30m/s wind flow over 45mm pit

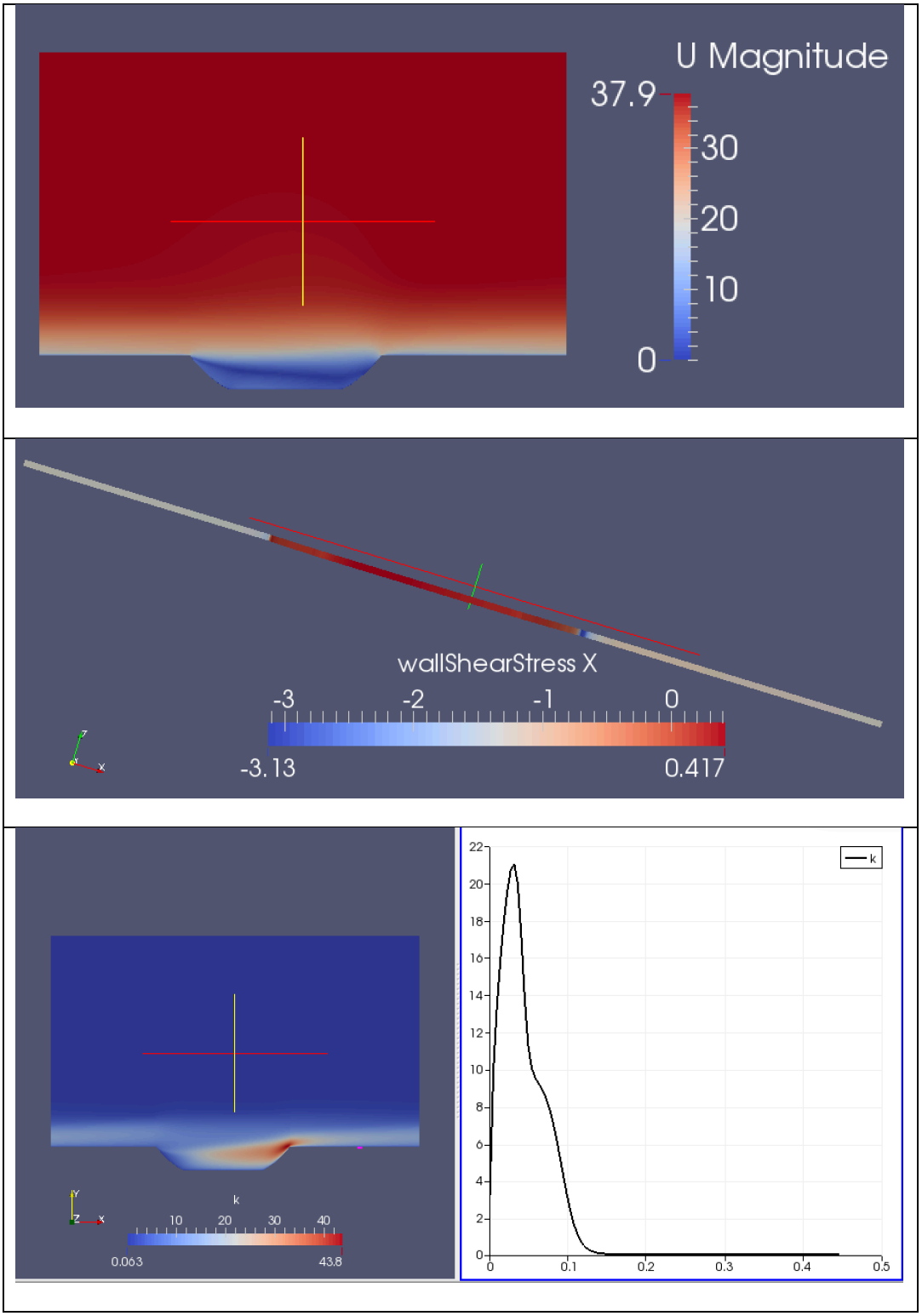

Velocity, shear stress, and turbulent kinetic energy of 35m/s wind flow over 45mm pit

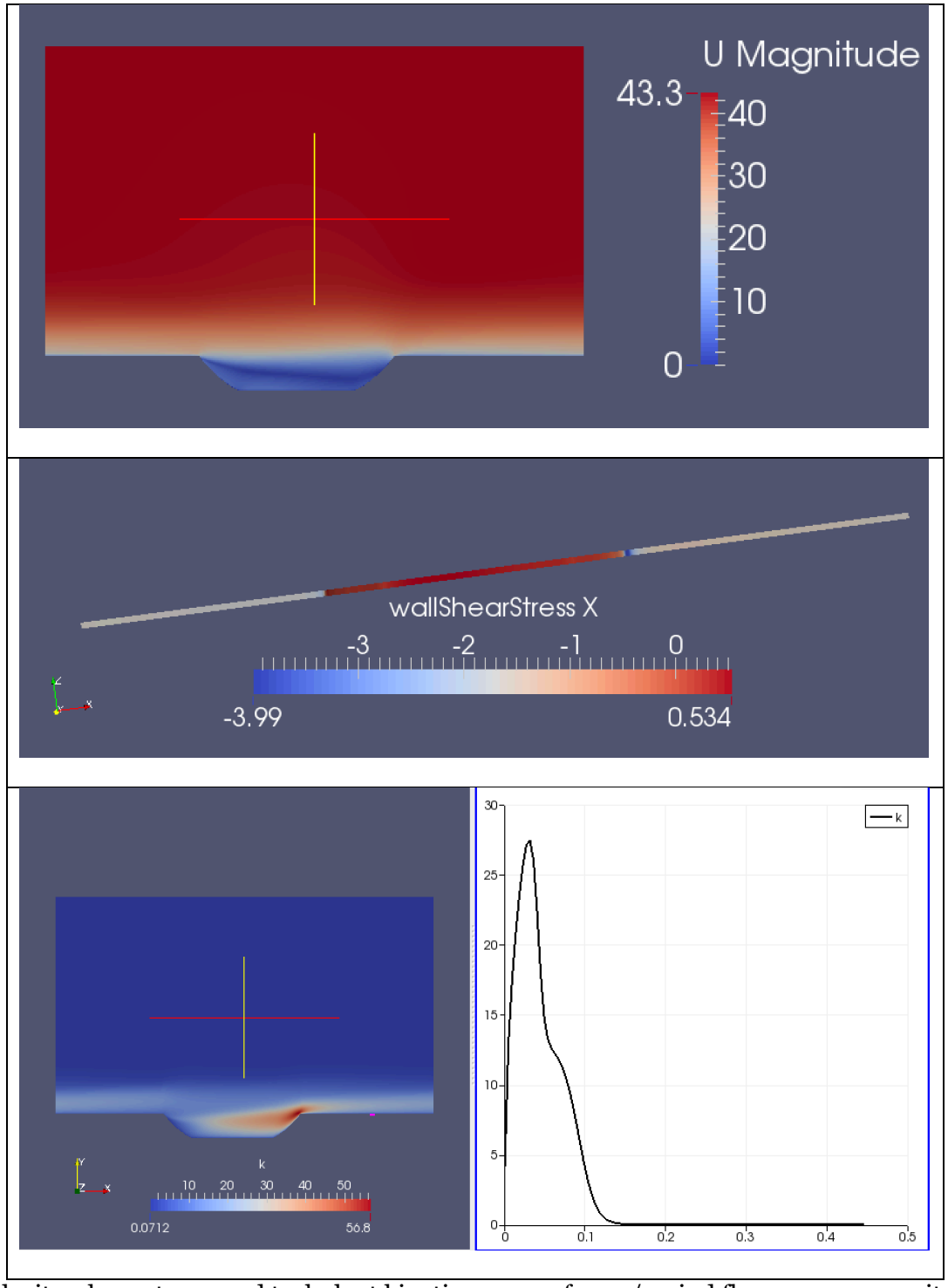

Velocity, shear stress, and turbulent kinetic energy of 40m/s wind flow over 45mm pit